

COMPOSITION- AND SIZE-CONTROLLED SYNTHESIS OF Mn-
Zn FERRITE NANOCRYSTALS FOR POTENTIAL
MAGNETOCALORIC APPLICATIONS

By

ERIC R. CALDERÓN ORTIZ

A thesis submitted in partial fulfillment of the requirements for the
degree of

MASTER OF SCIENCE
in
CHEMISTRY

UNIVERSITY OF PUERTO RICO
MAYAGÜEZ CAMPUS
2008

Approved by:

Carlos Rinaldi, Ph.D.
Member, Graduate Committee

Date

Felix Román, Ph.D.
Member, Graduate Committee

Date

Oscar Juan Perales Pérez, Ph.D.
President, Graduate Committee

Date

Gustavo Gutiérrez
Representative of Graduate Studies

Date

Francis Patrón, Ph.D.
Chairperson of the Department

Date

Rodolfo Romañach., Ph.D.
Member, Graduate Committee

Date

ABSTRACT

There are presently many applications using nanofluids in thermal engineering. Some examples include the use of nanoparticles in conventional coolants to enhance heat transfer rate by increasing its thermal conductivity. Other applications include the sealing of bearing cases and sealing of rotary shafts. Even at low weight concentration, thermal conductivity increases significantly. In biotechnology, magnetic nanoparticles have been proposed for thermal treatment of tumor using nanoshells and alternating magnetic fields to generate heat in localized points. This work evaluates the use of nanoparticles composed of $Mn_xZn_{1-x}Fe_2O_4$ ferrite for cooling applications in the room temperature range. The use of ferrimagnetic nanoparticles in a fluid, for cooling applications represents an encouraging alternative to traditional methods; the fact that the fluid with ours nanoparticles, can be pumped with no moving mechanical parts, using the magnetocaloric effect, can be a great advantage for many applications where maintenance or power consumption are undesirable. The magnetic material for this specific application has to have certain specific properties, like low Curie temperature (T_c), high saturation magnetization (M_s), low viscosity and high specific heat. The selection of this type of ferrite is made based on these properties. The synthesis of the ferrite nanoparticles was carried

out by chemical precipitation and the process is described further on. Magnetic characterization of $\text{Mn}_x\text{Zn}_{1-x}\text{Fe}_2\text{O}_4$ nanoparticles includes the determination of M_S as a function of composition at 300K and the dependence of M_S with temperature for a specific 'x' value. Both types of measurements were carried out by using SQUID (Superconducting Quantum Interference Device) magnetometer and VSM (Vibrating System Measurement).

RESUMEN

En la actualidad existen muchas aplicaciones con el uso de nano-fluidos en la ingeniería termal. Unos de los ejemplos incluyen el uso de nano-partículas en refrigerantes para incrementar la transferencia de calor aumentando la conductividad termal. Otras aplicaciones incluyen, la impermeabilización de cajas de compostura y la impermeabilización de ejes rotativos. Aún en concentraciones bajas en peso, la conductividad termal aumenta significativamente. En el campo de la biotecnología nano-partículas magnéticas han sido utilizadas para el tratamiento termal de tumores usando nano-capas y campos magnéticos alternos para la generación de calor en regiones específicas. Este trabajo evalúa el uso de nano-partículas de $Mn_xZn_{1-x}Fe_2O_4$ en fluido acuoso para aplicaciones de refrigerantes a temperatura ambiente. Este tipo de aplicación representa una alternativa innovadora para los métodos tradicionales es sistemas de enfriamiento; el hecho de que el fluido puede ser desplazado sin que partes mecánicas actúen sobre él, podría ser de gran avance para muchas aplicaciones donde el consumo de energía no es deseado. El material magnético deseado debe de presentar ciertas propiedades específicas como; baja Temperatura de Curie (T_C), alta magnetización de saturación (M_S), baja viscosidad y alto calor específico. La selección de las ferritas de Mn-Zn fue basada en estas propiedades. La síntesis de las nano-partículas fue hecha por

precipitación química y este proceso será explicado y descrito mas adelante. La caracterización magnética de las nano-partículas de $Mn_xZn_{1-x}Fe_2O_4$ incluye la determinación de M_S en función a la composición a 300K y la dependencia de M_S con temperatura para valores específicos de 'x'. Ambos tipos de medidas fueron llevadas a cabo usando los magnetómetros SQUID (Superconducting Quantum Interference Device) y VSM (Vibrating System Measurement) (por sus siglas en inglés).

Copyright © by
ERIC R. CALDERÓN ORTIZ
2008

ACKNOWLEDGEMENTS

During the development of my graduate studies in the University of Puerto Rico at Mayagüez several persons collaborated directly and indirectly with my research. Without their support it would be impossible for me to finish my work. I wish to dedicate this section of this thesis to recognize their help and support.

I want to start expressing thank you to a very important person in my life that always is there for me no matter what, my wife Carmen J. Melendez; without her, this work will never be done. Also, the person that start with all, Dr. Oscar Perales-Pérez, my advisor, because he gave me the opportunity to research under his guidance and supervision. I received motivation in the research area and all kind of support from him during all my studies. Special thanks to Dr. Rinaldi for be the first in gave me the opportunity of researching back in 2004, this opportunity started every thing, thank you.

Fundamental parts of my life are my father Rafael A. Calderón and my mother Nelly Ortiz, these two wonderful persons through all my life provide the help and support to me in order to achieve my success, mom and dad "**GRACIAS**". Also I want two say thanks to my brother

Jose A. Calderón for be there no matter what.

The grants from PREM and IDEAS NASA provided the funding for the initial part of the research, the other part of the work was funding by the Department of Defense of the United States of America for the continues of the required resources for the development of this research. Last but not less I want to thank all the members of Dr. Perales research group especially to Boris Rentaría and Celia Osorio for their help and collaboration during this process.

To my wife Judith and my son Eric Rafael

TABLE OF CONTENTS

<u>COMPOSITION- AND SIZE-CONTROLLED SYNTHESIS OF MN-ZN FERRITE NANOCRYSTALS FOR POTENTIAL MAGNETOCALORIC APPLICATIONS</u>	1
<u>ABSTRACT</u>	2
<u>RESUMEN</u>	4
<u>ACKNOWLEDGEMENTS</u>	7
<u>TABLE OF CONTENTS</u>	10
<u>LIST OF TABLES</u>	13
<u>LIST OF FIGURES</u>	14
<u>INTRODUCTION</u>	18
1.1 MOTIVATION	18
1.2 OBJECTIVES	22
1.2.1 GENERAL OBJECTIVE	22
1.2.2 SPECIFIC OBJECTIVES	22
1.3 CONTENTS OF THE THESIS	23
<u>THEORETICAL BACKGROUND</u>	24
1.4 INTRODUCTION TO MAGNETISM	24
1.4.1 ORIGIN OF MAGNETISM	24
BASIC CONCEPTS	26
1.4.2 TYPES OF MAGNETISM	32
I. DIAMAGNETISM	32
	10

II. PARAMAGNETISM AND SUPERPARAMAGNETISM	33
III. FERROMAGNETISM	34
DOMAINS AND HYSTERESIS	36
1.4.3 MAGNETIZATION AND TEMPERATURE	40
1.5 FERRITE	42
1.5.1 GENERAL PROPERTIES	42
1.5.2 FERRITES AND MAGNETOCALORIC PUMPING	46
1.5.3 RELATED WORKS ON SYNTHESIS AND MAGNETOCALORIC APPLICATIONS OF FERRITES	48
1.6 NUCLEATION AND GROWTH PROCESSES IN NANOSIZE CRYSTALS FORMATION	56
1.7 FUNDAMENTAL OF MATERIALS CHARACTERIZATION	57
1.7.1 X-RAY DIFFRACTION (XRD)	57
1.7.2 TRANSMISSION ELECTRON MICROSCOPY (TEM)	61
1.7.3 VIBRATING SAMPLE MAGNETOMETER (VSM)	66
1.7.4 SUPERCONDUCTING QUANTUM INTERFERENCE DEVICES (SQUID)	68
<u>METHODOLOGY</u>	<u>71</u>
1.8 MATERIALS	71
1.9 EXPERIMENTAL	71
1.10 CHARACTERIZATION.	74
<u>RESULTS AND DISCUSSION</u>	<u>75</u>
1.11 MN-ZN FERRITE NANOCRYSTALS	75
1.11.1 CONVENTIONAL CO-PRECIPIATION SYNTHESIS OF $MN_xZn_{1-x}Fe_2O_4$	75
1.11.2 MN-ZN FERRITE SYNTHESIS UNDER FLOW-RATE-CONTROLLED CONDITIONS	87
1.12 GADOLINIUM -DOPED MN-ZN FERRITE NANOCRYSTALS	95
1.12.1 CONVENTIONAL CO-PRECIPIATION SYNTHESIS OF $MN_xZn_{1-x}Fe_{2-y}Gd_yO_4$	
NANOCRYSTALS	95
1.12.2 FLOW-RATE CONTROLLED SYNTHESIS OF $MN_{0.8}Zn_{0.2}Fe_{1.99}Gd_{0.01}O_4$ FERRITE	
NANOCRYSTALS	104
1.12.2 MAGNETIC CHARACTERIZATION OF $MN_{0.8}Zn_{0.2}Fe_{1.99}Gd_{0.01}O_4$ FERRITE	
	11

NANOCRYSTALS 107

CONCLUDING REMARKS **111**

APPENDIX A **113**

REFERENCES **119**

LIST OF TABLES

Tabla 1.	Curie temperature of selected materials.	41
Tabla 2.	Radii of metal ions commonly involved in spinel ferrites.....	44
Tabla 3.	Magnetic properties of prepared magnetic fluid [19].....	49
Tabla 4.	Variation of magnetization in $Mn_{1-x}Zn_xFe_2O_4$ [20]	49
Tabla 5.	Co-Zn ferrite composition and magnetic properties [23].	52
Tabla 6.	Variation in average crystallite as a function of the atomic fraction of Mn ions in the $Mn_xZn_{1-x}Fe_2O_4$ ferrite.	77
Tabla 7.	Average Crystallite size and lattice parameter as a function of the differents value of the flow rate.....	89
Tabla 8.	Average crystallite size and maximun magnetization as a function of the flow rate of reactants additions.	92
Tabla 9.	Averagre crystallite size and lattice parameter, ‘a’, variation as a function of the Gd atomic fraction, ‘y’ in $Mn_{0.8}Zn_{0.2}Gd_yFe_{2-y}O_4$ nanocrystals.	97
Tabla 10.	Technical Curie temperature as a function of the atomic fraction of Gd ions, ‘y’.....	102
Tabla 11.	Average crystallite size and lattice parameter as a function of the flow rate for Gd-dope (y=0.01) ferrite.	106
Tabla 12.	ICP general data fr MN-Zn ferrite nanocrystals.....	113

LIST OF FIGURES

Figure 1.	Magnetic field generated around an electrical current loop. The ‘E’ represent the electrical current loops [5]	24
Figure 2.	A magnetic material can generate a magnetic field without an electric current. The blue lines represent the magnetic force of a magnet [5].....	25
Figure 3.	Magnetic field vector in space.....	27
Figure 4.	Representation of two magnetic field vector.....	28
Figure 5.	(a) Electron orbit around the nucleus (b) Electron spin.....	31
Figure 6.	The atomic configuration for diamagnetic material with and with out a magnetic field. The represent the external magnetic field applied	32
Figure 7.	Atomic dipole configuration with and without an external magnetic field for a paramagnetic material.....	34
Figure 8.	Schematic illustration of the mutual alignment of atomic dipole for a ferromagnetic material when an external magnetic field is applied.	35
Figure 9.	(a) Ferrimagnetic and (b) antiferromagnetic behavior with and without external magnetic field.	36
Figure 10.	Variation in magnetization and domains under an external field.....	38
Figure 11.	Magnetic flux density versus the magnetic field strength for. ‘M’ represent the magnetization, ‘H’ represent the external magnetic field applied and the ‘ M_s ’ is the saturation magnetization of the material.	39
Figure 12.	Typical M-T curve for magnetic materials.....	40
Figure 13.	The ferrite structure. A and B are the tetrahedral and octahedral sites.	43
Figure 14.	Scheme of a magnetocaloric pumping system. The letter <i>a</i> represent the zone were the cool magnetic fluid will enter, <i>b</i> is the	

	heating zone and c the exit zone of the magnetic fluid at higher temperature	47
Figure 15.	Classical model proposed by LaMer and Dinegar to explain the mechanism of formation of colloids [30]	56
Figure 16.	XRD Siemens D500 unit at the Department of Engineering Science and Materials UPRM.	58
Figure 17.	Basic features of a typical XRD experiment.	59
Figure 18.	Atomic planes and their d-spacings in a simple cubic (SC) unit cell.	60
Figure 19.	Miller indices of atomic planes in a SC unit cell.....	61
Figure 20.	TEM Philips CM200 UT CM200 UT at the Department of Materials Science & Engineering, University of Wisconsin.....	62
Figure 21.	Schematic diagram of a TEM instrument, showing the location of a thin sample and the principal lenses within a TEM column [36].....	63
Figure 22.	Schematic representation for the ray paths of both unscattered and scattered electrons beneath the sample.....	65
Figure 23.	Lake Shore 7400 Series VSM at the Department of Engineering Science & Materials at UPRM.	66
Figure 24.	(a) Schematic diagram of a vibrating coil magnetometer and (b) schematic diagram of a vibrating sample magnetometer.	67
Figure 25.	(a) Quantum Design MPMSXL available at UPRM and (b) schematic diagram of the SQUID unit.	69
Figure 26.	Experimental procedure for the synthesis of Mn-Zn ferrite nanocrystals.	73
Figure 27.	XRD patterns for Mn-Zn ferrites synthesized on a hot plate at different Mn atomic fraction 'x'	76
Figure 28.	HRTEM images of $Mn_{0.7}Zn_{0.3}Fe_2O_4$ nanocrystals at different magnifications.	80
Figure 29.	Room temperature M-H loops for $Mn_xZn_{1-x}Fe_2O_4$ ferrites synthesized at different Mn atomic fractions, 'x'.....	82
Figure 30.	Magnetization and Average Crystallite size as a function of Mn	

	atomic fraction.....	83
Figure 31.	M-T plots for $Mn_xZn_{1-x}Fe_2O_4$ ferrites at different Mn atomic fractions, 'x'. The external magnetic field was 2.2 Tesla.....	85
Figure 32.	Variation of the technical Curie temperature with the Mn atomic fraction, 'x' in $Mn_xZn_{1-x}Fe_2O_4$ nanocrystals.....	86
Figure 33.	XRD patterns for Mn-Zn ferrites, 'x'= 0.8 for Mn, synthesized under intensive heating and different flow-rate of the addition of the reactants. For comparison purposes, the pattern for the solid produced with no control on flow-rate ('0' mL/min) is also presented.....	88
Figure 34.	Room temperature M-H Curves for Mn-Zn ferrites (x=0.8) synthesized under flow-rate controlled conditions. '0' mL/min corresponds to the solid produced with no control of the flow rate of reactant addition.	91
Figure 35.	M-T Curves for Mn-Zn ferrites for different rate addition of ionic solutions "flow rate control". The external magnetic field was 2.2T.....	94
Figure 36.	XRD patterns for Gd-doped $Mn_{0.8}Zn_{0.2}Gd_yFe_{2-y}O_4$ synthesized on a hot plate and at different Gd atomic fractions, 'y'.	96
Figure 37.	Room temperature M-H curve for Gd-doped $Mn_{0.8}Zn_{0.2}Fe_{2-y}Gd_yO_4$ at different Gd atomic fraction, 'y'. The inset shows the Maximum Magnetization values for different the atomic fractions of Gd, 'y'	98
Figure 38.	M-T plots for $Mn_{0.8}Zn_{0.2}Fe_{2-y}Gd_yO_4$ ferrites at different Gd atomic fractions, 'y'. The external magnetic field was 7 T.....	101
Figure 39.	M-T plots for Mn(0.08)-Zn ferrites with and without Gd ions ('y'=0.01). The external magnetic field was 2.2 T.....	103
Figure 40.	XRD patterns for $Mn_{0.8}Zn_{0.2}Gd_yFe_{2-y}O_4$ doped with Gd y=0.01, synthesized at different flow rate of the reactants addition.....	105
Figure 41.	Room temperature M-H Curves for Mn(0.08)-Zn ferrites doped with Gd and synthesized at different flow-rates.....	108
Figure 42.	M-T Curves for Mn-Zn (x=0.8, y=0) ferrite nanocrystals and Gd-	

doped Mn-Zn ferrite nanocrystals ($x=0.8$, $y=0.01$) synthesized with and without control on flow-rate (10mL/min). The external magnetic field was 2.2 T. 110

INTRODUCTION

1.1 MOTIVATION

Nanometer sized magnetic particles are the subject of intense research because of their potential applications in high-density magnetic recording, magnetic fluids, etc. Stable aqueous suspensions of ferrite nanoparticles are needed in the so-called 'magneto-caloric energy conversion'. In this process, a magnetic fluid bearing suspension is heated, loses its magnetization and can then be displaced by cooler fluid, i.e., the magnetic suspension will flow with no moving mechanical parts [1]. Accordingly, magnetocaloric energy conversion provides a simple means of pumping fluid using only external thermal and magnetic fields. The impact of such a phenomenon is obvious: fluid propulsion with no moving mechanical parts. Based on the fact that the closer the temperature of the magnetic fluid to the Curie temperature of the ferrite, the higher the pressure gradient responsible for the flow, the candidate material should have a Curie temperature (T_C) close enough to the maximum operating temperature. This condition will make sure that the ferrite should exhibit a suitable reduction in its magnetization. Accordingly, the Curie temperature of the water-based ferrite suspension to be used in magneto-caloric applications should be as close

as possible to 100°C (operating temperature range). Although magnetite, Fe_3O_4 , has been commonly used in most magnetic fluid formulations, its Curie temperature (585°C) is far above expected operating temperatures. Under this condition, most of the solvent (water, for instance) will be evaporated before the temperature would reduce the ferrite magnetization. Among ferrite materials, Mn-Zn ferrite has been reported to have Curie temperatures between 75°C and 325°C [2]-[3] for polydisperse crystals ranging in size between 6nm and 20nm. The replacement of Mn ions from the tetrahedral A-site with a non-magnetic ion such as Zn in the ferrite structure will result in the reduction of the exchange interaction between Mn ions with Fe in the ferrite octahedral B-sites. Accordingly, a decrease in the Curie temperature and an increase in saturation magnetization can be expected, providing the cation distribution. In case of Gd-ferrite exhibits a Curie temperature as low as 298K and high pyromagnetic coefficient [2] could open the possibility to tune the T_C in Mn-Zn ferrites by a controlled incorporation of this rare-earth element into the ferrite structure. Tunability of Curie temperature would favor a further enhancement of the pressure gradient in the corresponding magnetocaloric system. In turn, it has been found that the incorporation of Gd(III) species into the Mn-Zn ferrite structure can also increase the saturation magnetization of the corresponding magnetic fluid and hence,

the pyromagnetic coefficient of the magnetic fluid, $\Delta M/\Delta T$ [2], keeping the volume fraction of ferrite in the fluid constant. The increase in magnetization was attributed to the substitution of B-site Fe by Gd ion. Although this effect is reported, there is neither detailed evaluation nor discussion describing how the magnetization and pyromagnetic coefficient would depend on composition and crystal size in the Gd-doped systems.

On the above basis, the present research will be focused on the development of optimum ferrite materials for magnetocaloric systems. Magnetic properties of selected materials (saturation magnetization, T_C , and pyromagnetic coefficient) will be optimized under a composition-, structure- and size-controlled conditions. The variation in those magnetic properties will be attempted by promoting atomic rearrangements between the tetrahedral (A) and octahedral sites (B) in the ferrite structure. For this purpose, $Mn_{1-x}Zn_xFe_2O_4$, where 'x' varying from 0.0 to 1.0, will be synthesized in aqueous phase. Ferrite nanoparticles having optimum magnetic properties, will be then doped with rare earth species (Eu and Gd) at different atomic fractions 'y' ($y = 0.01$ to 0.1 in $Mn_{1-x}Zn_xFe_{2-y}RE_yO_4$, where RE = rare earth ions) and magnetically characterized as a function of composition and crystal size. The presence of the rare earth ions should increase the occupancy of Mn

ions in A-sites, which in turn will affect both, the T_c and the corresponding pyromagnetic coefficient. In order to increase the magnetic properties like M_S and understand the effect in the T_c , it is attempt to increase the crystal size of the nanoparticles by controlled the addition of ionic solution in to the alkaline solution. The controlled addition of the ionic solution is called flow rate control.

1.2 OBJECTIVES

The present research will explore the following objectives.

1.2.1 General Objective

To investigate the effect of composition and crystal size on the magnetic properties of Mn-Zn ferrite nanocrystals with and without Gd(III) doping.

1.2.2 Specific Objectives

1. To determine the optimum synthesis conditions for Mn-Zn ferrite (undoped and rare-earth-doped) nanocrystals in aqueous phase.
2. To develop specific methods to enhance crystal growth at the nanoscale.
3. To characterize ferrite nanocrystals from a structural, compositional and morphological point of view.
4. To determine the magnetic properties (Magnetization and Magnetization-Temperature behavior) of $\text{Mn}_x\text{Zn}_{1-x}\text{Fe}_2\text{O}_4$ ferrite nanocrystals, where 'x' is the atomic Mn fraction.
5. To determine the magnetic properties (Magnetization and Magnetization-Temperature behavior) of $\text{Mn}_x\text{Zn}_{1-x}\text{Fe}_{2-y}\text{Gd}_y\text{O}_4$ ferrite nanocrystals.

1.3 CONTENTS OF THE THESIS

Chapter 1 includes the introduction and the objectives of the present thesis. The theoretical background, which includes the fundamentals of magnetism, general information on the ferrite materials as well as the basics of the characterization techniques will be presented in chapter 2. The methodology is the next part of this thesis and is presented in chapter 3. This section also includes details of the experimental procedure. Chapter 4 presents the main findings of the research and the corresponding interpretation. The concluding remarks are summarized in Chapter 5.

THEORETICAL BACKGROUND

1.4 INTRODUCTION TO MAGNETISM

1.4.1 Origin of magnetism

A very simple way to see what magnetism is with the interaction of certain materials. In this physical phenomenon an electric current loop generates a region of physical attraction, or magnetic field represented by a magnetic flux line. In figure 1 is showed a simple illustration of this phenomenon.

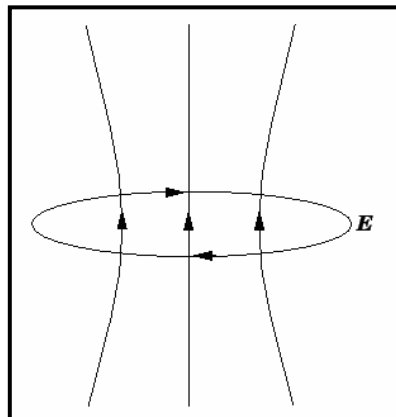


Figure 1. Magnetic field generated around an electrical current loop. The 'E' represent the electrical current loops [5]

The magnetic field vector at any given point near to the electric current loop is given by H , vector quantity. There also other type of materials that are inherently magnetic, that is, they can generate magnetic field

without a macroscopic electric current [5].

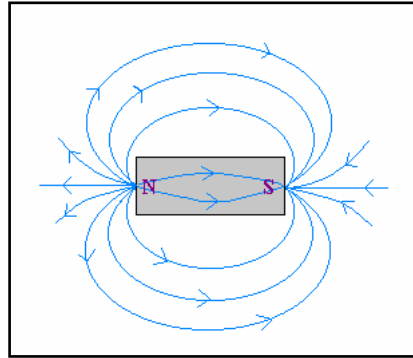


Figure 2. A magnetic material can generate a magnetic field without an electric current. The blue lines represent the magnetic force of a magnet [5].

Figure 2 presents a magnetic bar as an example, exhibits an identifiable dipole north –south that give the orientation. The best utility of magnetism is the force of attraction that can provide. Many of our present technology devices relied on magnetism and magnetic materials; these include electrical power generators and transformers, electric motors, radio, television, telephone, computer and other component of sound and videos [5].

Mother Nature also gives materials like iron, some steels and naturally minerals that exhibit magnetic properties. Not so that familiar is the fact that all substances are influenced to one degree or another by the presence of magnetic field.

BASIC CONCEPTS

Magnetic Dipoles

In physics, there are two kinds of dipoles, an electric dipole is a separation of positive and negative charge. The simplest example of this is a pair of electric charges of equal magnitude but opposite sign, separated by some, usually small, distance. By contrast, a magnetic dipole is a closed circulation of electric current. A simple example of this is a single loop of wire with some constant current flowing through it [6].

Dipoles can be characterized by their dipole moment, a vector quantity. For the simple electric dipole given above, the electric dipole moment would point from the negative charge towards the positive charge, and have a magnitude equal to the strength of each charge times the separation between the charges. For the current loop, the magnetic dipole moment would point through the loop (according to the right hand rule), with a magnitude equal to the current in the loop times the area of the loop.

In addition to current loops, the electron, among other fundamental particles, is said to have a magnetic dipole moment. This is because it generates a magnetic field which is identical to that generated by a very small current loop. However, to the best of our knowledge, the electron's magnetic moment is not due to a current loop, but is instead an intrinsic property of the electron. It is also possible that the electron

has an electric dipole moment, although this has not yet been observed. A permanent magnet, such as a bar magnet, owes its magnetism to the intrinsic magnetic dipole moment of the electron. The two ends of a bar magnet are referred to as poles (not to be confused with monopoles), and are labeled "north" and "south." The dipole moment of the bar magnet points from its magnetic south to its magnetic north pole—confusingly, the "north" and "south" convention for magnetic dipoles is the opposite of that used to describe the Earth's geographic and magnetic poles, so that the Earth's geomagnetic north pole is the south pole of its dipole moment.

The only known mechanisms for the creation of magnetic dipoles are by current loops or quantum-mechanical spin since the existence of magnetic monopoles has never been experimentally demonstrated.

Magnetic Field Vectors

The magnetic field at any point in space is a vector quantity. This means there is a direction associated with the field as well as field strength.

Consider the arrow below:

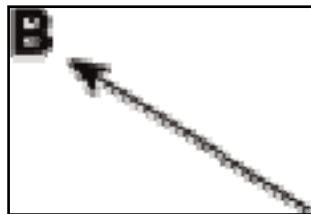


Figure 3. Magnetic field vector in space.

The direction of the arrow can be thought of as the direction of the magnetic field. The length of the arrow can be thought of as the strength of the field, i.e. the longer the arrow, the stronger the field. Call this length, B .

If a set of axes is placed on the arrow, it can divide the field into two components of the field, namely the x component and the y component. Call these lengths, B_x and B_y .

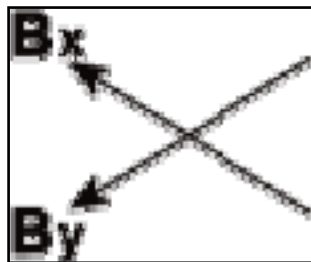


Figure 4. Representation of two magnetic field vector.

Now, the length of the arrow can be described, or the strength of the magnetic field, in terms of the x and y components. Using the Pythagorean Theorem:

$$B = \sqrt{B_x^2 + B_y^2} \quad \text{Equation (1)}$$

Now imagine that there exists a third direction, so that the arrow, B can be pointing out of (or into) the plane of the page. There is now a third component, namely B_z , which in the example is the length of the component stretching from the page outward to the tip of the arrow.

By exactly the same mathematics, now B is described as:

$$B = \sqrt{B_x^2 + B_y^2 + B_z^2} \quad \text{Equation (2)}$$

The value B, is the strength of the magnetic field. B_x , B_y , and B_z are the three components measured by a three axis. A single axis measuring device will change its reading depending on which way the sensitive axis is oriented with respect to the direction of the magnetic field. To obtain a complete representation of magnetic field at any point in space, one needs not only the value of B, but the direction, which can be expressed as the three components, B_x , B_y and B_z .

Origins of Magnetic Moments

The magnetic moment or magnetic dipole moment is a measure of the strength of a magnetic source. In the simplest case of a current loop, the magnetic moment is defined as:

$$m = I \int da \quad \text{Equation (3)}$$

where a is the vector area of the current loop, and the current, I is a constant. By convention, the direction of the vector area is given by the right hand rule.

In the more complicated case of a spinning charged solid, the magnetic moment can be found by the following equation:

$$m = \frac{1}{2} \int r \times J d\tau \quad \text{Equation (4)}$$

where

$$dr = r^2 \sin \theta d\tau d\theta d\phi$$

and J is the current density.

The magnetic moment in a magnetic field is a measure of the magnetic flux set up by the gyration of an electric charge in a magnetic field. The moment is negative, indicating it is diamagnetic, and equal to the energy of rotation divided by the magnetic field.

In atomic and nuclear physics, the symbol m represents moment, measured in Bohr magnetons, associated with the intrinsic spin of the particle and with the orbital motion of the particle in a system, also called magnetic dipole moment. For a system of charges, the magnetic moment is determined by summing the individual contributions of each charge-mass-radius component.

Electron Spin

With the concept of electron spin introduced by Goudsmit in 1925 and Uhlenbeck in 1926, the origin of magnetism was explained. Spin corresponds to movement of electric charge in the electron, hence an electric current which produces a magnetic moment in the atom. The net magnetic moment is the vector sum of the individual spin and orbital moments of the electrons in the outer shells [7]. Next figure illustrates these two phenomena:

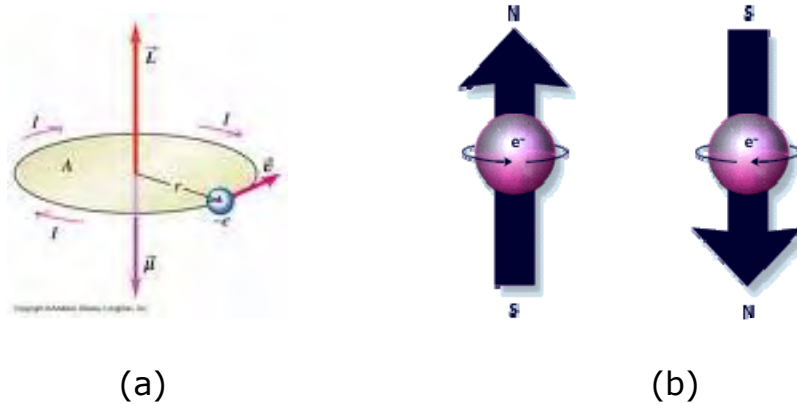


Figure 5. (a) Electron orbit around the nucleus (b) Electron spin

The electron spin can be represented in two modes pointed up or down. In an atom, with opposed paired spins cancel and do not result in magnetic moment, while the unpaired spins will give rise to a net magnetic moment.

1.4.2 Types of magnetism

I. DIAMAGNETISM

Diamagnetism is a weak repulsion from a magnetic field. It is a form of magnetism that is only exhibited by a substance in the presence of an externally applied magnetic field. It results from changes in the orbital motion of electrons. Applying a magnetic field creates a magnetic force on a moving electron in the form of $F = Qv \times B$. This force changes the centripetal force on the electron, causing it to either speed up or slow down in its orbital motion. This changed electron speed modifies the magnetic moment of the orbital in a direction opposing the external field. In the absence of an external field, no dipoles exist; in the presence of a field, dipoles are induced that are aligned opposite to the field direction [5]. Figure 6 show the behavior of a diamagnetic material with an applied magnetic field.

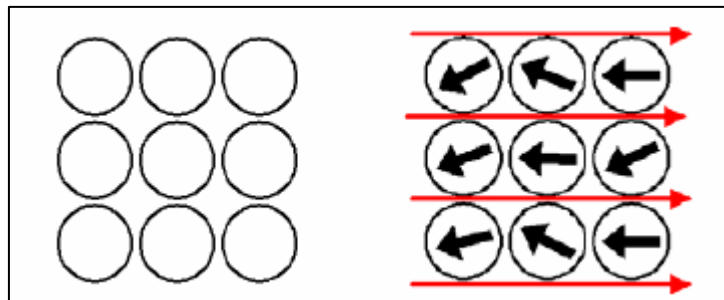


Figure 6. The atomic configuration for diamagnetic material with and with out a magnetic field. The  represent the external magnetic field applied

II. PARAMAGNETISM AND SUPERPARAMAGNETISM

Paramagnetism is a form of magnetism which occurs only in the presence of an externally applied magnetic field. Paramagnetic materials are attracted to magnetic fields; hence have a relative magnetic permeability greater than one (or, equivalently, a positive magnetic susceptibility). However, unlike ferromagnets which are also attracted to magnetic fields, paramagnets do not retain any magnetization in the absence of an externally applied magnetic field. Superparamagnetism is a phenomenon by which magnetic materials may exhibit a behavior similar to paramagnetism even when at temperatures below the Curie temperature. This is a small length-scale phenomenon, where the energy required to change the direction of the magnetic moment of a particle is comparable to the room thermal energy. At this point, the rate at which the particles will randomly reverse direction becomes significant.

Materials that are paramagnetic become magnetized in the same direction as that of an applied magnetic field and the amount of magnetization is proportional to that of the applied magnetic field. Figure 7 shows the behavior of a paramagnetic material without a magnetic field [8-12]

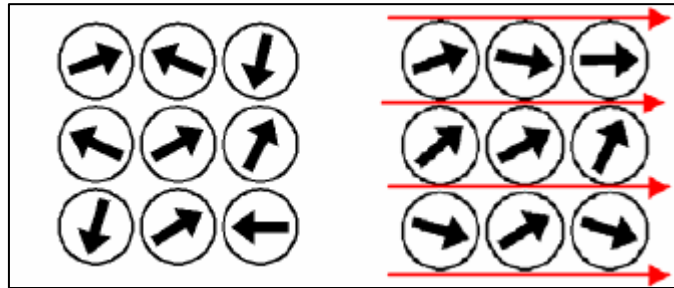


Figure 7. Atomic dipole configuration with and without an external magnetic field for a paramagnetic material.

III. FERROMAGNETISM

Ferromagnetism is the "normal" form of magnetism which most people are familiar with, as exhibited in horseshoe magnets and refrigerator magnets, for instance. It is responsible for most of the magnetic behavior encountered in everyday life. The attraction between a magnet and ferromagnetic material is "the quality of magnetism first apparent to the ancient world, and to us today" according to a classic text on ferromagnetism [13]. Ferromagnetism is defined as the phenomenon by which materials, such as iron, in an external magnetic field become magnetized and remain magnetized for a period after the material is no longer in the field. Ferromagnetic materials have atomic magnetic fields that align themselves parallel to externally applied magnetic fields. This creates a total magnetic field within the material much greater than the applied field. Above a critical temperature known as the Curie temperature, the material becomes paramagnetic [10]. Figure 8 shows

the behavior of a ferromagnetic material, which will exist even in the absence of an external magnetic field [5].

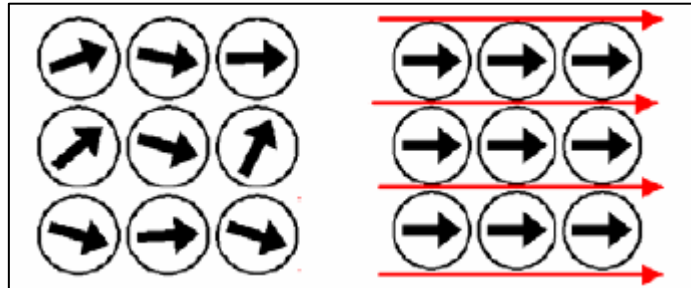


Figure 8. Schematic illustration of the mutual alignment of atomic dipole for a ferromagnetic material when an external magnetic field is applied.

IV. ANTIFERROMAGNETISM AND FERRIMAGNETISM

Antiferromagnetic materials have a natural state in which the atomic magnetic fields are arranged anti-parallel within the material. The anti-parallel magnetic fields are opposite and equal resulting in no net external magnetic fields. This natural state makes it difficult for the material to become magnetized in the direction of the applied field but still demonstrates a relative permeability slightly greater than 1. Above a critical temperature known as the Neel temperature, the material becomes paramagnetic [12].

Materials that are ferrimagnetic have atomic magnetic fields that align themselves both parallel and anti-parallel to the externally applied magnetic field. The parallel components are stronger than the anti-parallel components resulting in a net parallel magnetic field that can be

substantial. While these materials may also demonstrate a relative permeability greater than 1, their temperature dependencies are not as consistent as with ferromagnetic materials and can result in some very unusual results [12]. Figure 9 shows the behavior of a ferromagnetic and antiferromagnetic material.

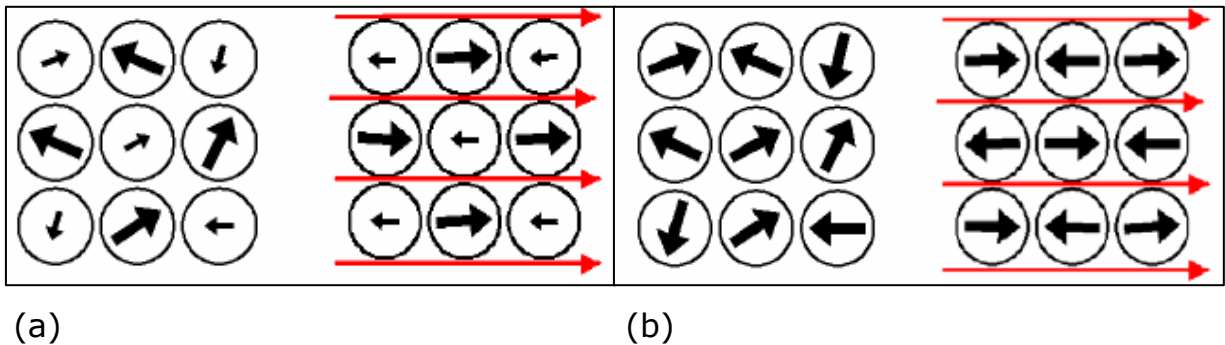


Figure 9. (a) Ferrimagnetic and (b) antiferromagnetic behavior with and without external magnetic field.

DOMAINS AND HYSTERESIS

In magnetism, a domain wall is an interface separating magnetic domains. It is a transition between different magnetic moments and usually undergoes an angular displacement of 90° or 180° . Although they actually look like a very sharp change in magnetic moment orientation, when looked at in more detail there is actually a very gradual reorientation of individual moments across a finite distance [14].

The energy of a domain wall is simply the difference between the magnetic moments before and after the domain wall was created. This

value is more often than not expressed as energy per unit wall area.

The width of the domain wall varies due to the two opposing energies that create it: the Magnetocrystalline anisotropy energy and the exchange energy, both of which want to be as low as possible so as to be in a more favorable energetic state. The anisotropy energy is lowest when the individual magnetic moments are aligned with the crystal lattice axes thus reducing the width of the domain wall, whereas the exchange energy is reduced when the magnetic moments are aligned parallel to each other and thus makes the wall thicker, due to the repulsion between them (where anti-parallel alignment would bring them closer - working to reduce the wall thickness). In the end equilibrium is reached between the two and the domain wall's width is set as such.

An ideal domain wall would be fully independent of position; however, they are not ideal and so get stuck on inclusion sites within the medium, also known as crystallographic defects. These include missing or different (foreign) atoms, oxides, and insulators and even stresses within the crystal. This prevents the formation of domain walls and also inhibits their propagation through the medium. Thus a greater applied magnetic field is required to overcome these sites. Figure 10 illustrates the domain walls in a magnetic material [15].

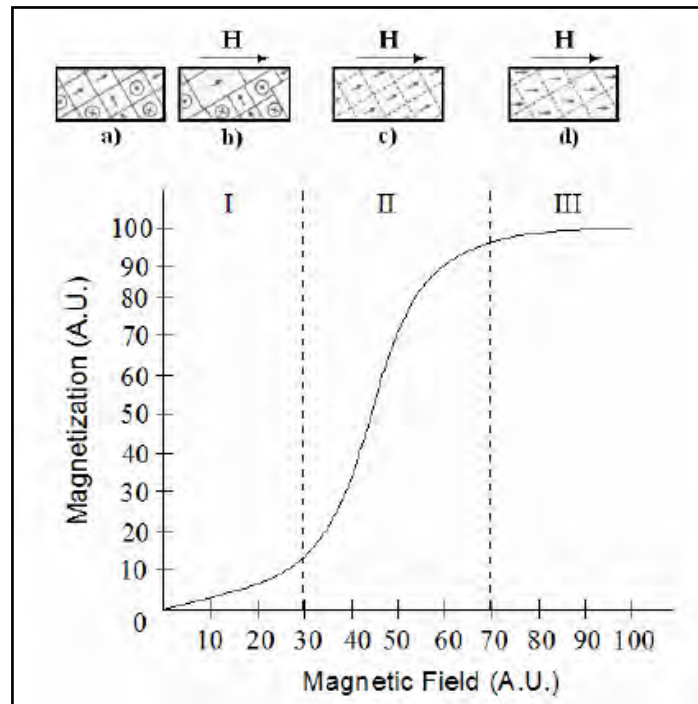


Figure 10. Variation in magnetization and domains under an external field.

Hysteresis phenomena occur in magnetic and ferromagnetic materials, as well as in the elastic and electromagnetic behavior of materials, in which a lag occurs between the application and the removal of a force or field and its subsequent effect. Electric hysteresis occurs when applying a varying electric field and elastic hysteresis occurs in response to a varying force. The term "hysteresis" is sometimes used in other fields, such as economics or biology. In such cases it describes a memory or lagging effect in which the order of previous events can influence the order of subsequent events. A hysteresis effect is produced in which the B field lags behind the applied H field, or decreases at a lower rate [5]. When the H field is zero a residual B field is presented, that is called the

remanence , or the remanence flux density M_r . This mean that the material remains magnetized in the absence of an external field. To reduce the B field within the specimen to zero an H field of magnitude H_c must de applied in a direction opposite to that of the original field; H_c is called the coercivity, or sometime the coercive force. Finally when all the magnetic vectors are in the same direction of the external magnetic field this point in the hysteresis curve is call saturation magnetization M_s . Ferri- or superparamagnetic materials do not exhibit coercivity. Figure 11 shows the M-H curve for a typical ferromagnetic material, like our Mn-Zn ferrite nanocrystals.

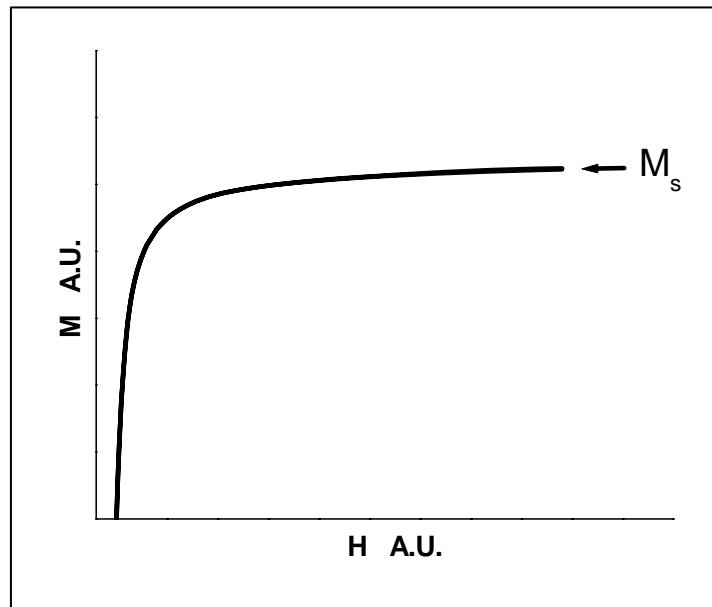


Figure 11. Magnetic flux density versus the magnetic field strength for. 'M' represent the magnetization, 'H' represent the external magnetic field applied and the ' M_s ' is the saturation magnetization of the material.

1.4.3 Magnetization and Temperature

The influence of temperature on magnetic material can be determined in the magnetic properties of those materials. Raising the temperature of a solid, results in the increase of the thermal vibrations of atoms, with this the atomic magnetic moments are free to rotate. This phenomenon the atoms tend to randomize the directions of any moments that may be aligned [5]. With increasing temperature, the saturation magnetization diminishes gradually and abruptly drops to zero at what is called the Curie temperature (T_c)

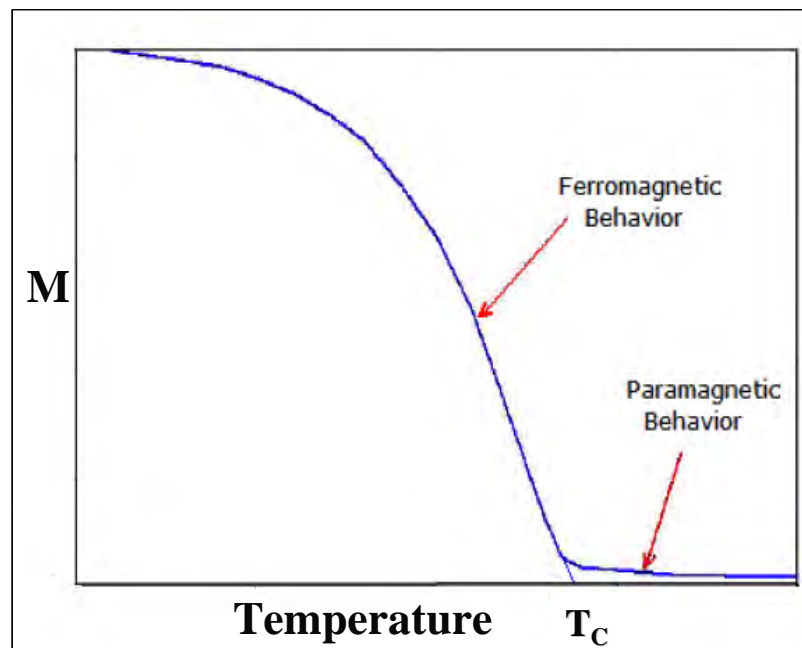


Figure 12. Typical M-T curve for magnetic materials.

The Curie point of a ferromagnetic material is the temperature above which it loses its characteristic ferromagnetic ability. At temperatures

below the Curie point the magnetic moments are partially aligned within magnetic domains in ferromagnetic materials. As the temperature is increased from below the Curie point, thermal fluctuations increasingly destroy this alignment, until the net magnetization becomes zero at and above the Curie point. Above the Curie point, the material is purely paramagnetic.

At temperatures below the Curie point, an applied magnetic field has a paramagnetic effect on the magnetization, but the combination of paramagnetism with ferromagnetism leads to the magnetization following a hysteresis curve with the applied field strength. Table 1 shows some examples of Curie temperature for various materials.

Material	Curie temperature (K)
Gadolinium	292
Nickel	631
Magnetite	858
Iron	1043
Cobalt	1393

Tabla 1. Curie temperature of selected materials.

For the present work, we will use a 'Technical Curie temperature' that will be defined as the temperature at which the magnetization of compacted ferrite nanocrystals will be zero under the influence of a fixed

external magnetic field (2.2 T in VSM and 7 T in a SQUID magnetometer). The effect of inter-particle magnetic interactions (as required when dealing with actual Curie temperature values in bulk magnetic materials) will not be considered under this practical definition.

1.5 FERRITE

1.5.1 General Properties

Ferrites are a class of chemical compounds with the formula AB_2O_4 , where A and B represent various metal cations, usually including iron. These ceramic materials are used in applications ranging from magnetic components in microelectronics.

These are the type of materials that adopt a crystal motif consisting of cubic close-packed (FCC) oxides (O^{2-}) with A cations occupying one eighth of the tetrahedral holes and B cations occupying half of the octahedral holes. The magnetic material known as "ZnFe" has the deceptively simple formula $ZnFe_2O_4$, with Fe^{3+} occupying the octahedral sites and half of the tetrahedral sites. The remaining tetrahedral sites in this spinel are occupied by Zn^{2+} [16]. These A and B sites are illustrated in Figure 13. In total, there are 64 tetrahedral sites and 32 octahedral sites in the unit cell, of which only 8 tetrahedral sites and 16 octahedral sites are occupied, resulting in a structure that is electrically neutral.

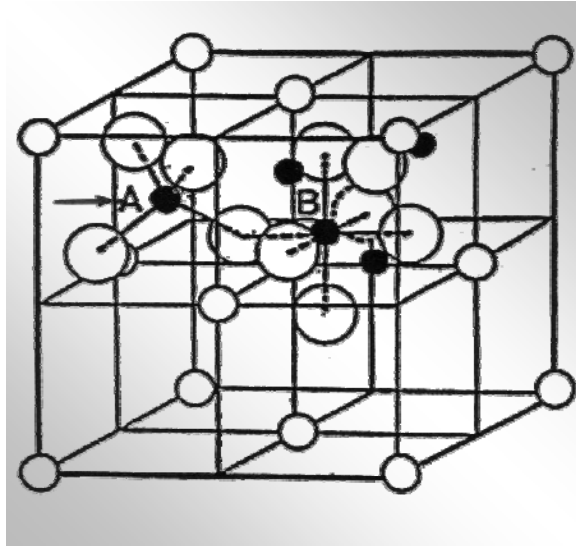


Figure 13. The ferrite structure. A and B are the tetrahedral and octahedral sites.

There are two types of spinel structure: normal and inverse. In the case of the normal spinel, the divalent ions are all on A sites and trivalent ions occupy B sites. A majority of these ferrites present paramagnetic behavior. In the inverse spinel, the divalent ions occupy only B sites while trivalent ions are located on both A and B sites in equal proportion. The spin moments of the trivalent ions in an inverse spinel are canceled (direction of moment on A sites is opposed to B sites) whereas the spin moments of the divalent ions are aligned, resulting in a net magnetic moment [17].

Ion	Ionic radius (Å)
Fe ²⁺	0.83
Fe ³⁺	0.67
Fe ²⁺	0.70
Co ²⁺	0.82
Zn ²⁺	0.74
Ni ²⁺	0.78

Tabla 2. Radii of metal ions commonly involved in spinel ferrites.

General Applications of Ferrites

Ferrites are usually non-conductive ferrimagnetic ceramic compounds derived from iron oxides such as hematite (Fe₂O₃) or magnetite (Fe₃O₄) as well as oxides of other metals. Ferrites are, like most other ceramics, hard and brittle. In terms of the magnetic properties, ferrites are often classified as "soft" and "hard" which refers to their low or high coercivity of their magnetism, respectively. Ferrites that are used in transformer or electromagnetic cores contain nickel, zinc, or manganese compounds. They have a low coercivity and are called soft ferrites. Because of their comparatively low losses at high frequencies, they are extensively used in the cores of Switched-Mode Power Supply (SMPS) and RF transformers and inductors. A common ferrite, abbreviated MnZn is composed of the oxides of manganese and zinc. Also this type of

ferrite has low coercivity, low remanence and high saturation magnetization, the last one very important for the magnetocaloric application.

In contrast, permanent ferrite magnets (or "hard ferrites") are composed of iron and barium or strontium oxides. In a magnetically saturated state they conduct magnetic flux well and have a high magnetic permeability. This enables these so-called ceramic magnets to store stronger magnetic fields than iron itself. They are the most commonly used magnets in radios. The maximum magnetic field B is about 0.35 tesla and the magnetic field strength H is about 30 to 160 kA turns per meter (400 to 2000 Oe) [18].

Ferrite cores are used in electronic inductors, transformers, and electromagnets where the high electrical resistance of the ferrite leads to very low eddy current losses. They are commonly seen as a lump in a computer cable, called a ferrite bead, which helps to prevent high frequency electrical noise (radio frequency interference) from exiting or entering the equipment. Early computer memories stored data in the residual magnetic fields of hard ferrite cores, which were assembled into arrays of core memory. Ferrite powders are used in the coatings of magnetic recording tapes. One such type of material is iron (III) oxides. Ferrite particles are also used as a component of radar-absorbing materials or coatings used in stealth aircraft and in the expensive

absorption tiles lining the rooms used for electromagnetic compatibility measurements. Most common radio magnets, including those used in loudspeakers, are ferrite magnets.

1.5.2 Ferrites and Magnetocaloric Pumping

A magnetocaloric pump provides a simple way of pumping fluid using only heat transfer and a magnetic field. The working principle is simple: magnetic materials lose magnetization as their temperature increases, reaching a point where they can no longer maintain a spontaneous magnetization, this temperature is called the Curie temperature. Figure 14 shows a typical magnetization vs. temperature curve for a given material with the y axis is expressed as the ratio between the magnetization at any temperature (M) and the saturation magnetization at a temperature of 0 K, $M(T)/M_s(0K)$, and the x axis is the temperature normalized with the Curie temperature, $T(K)/T_c(K)$ [5].

When a ferrofluid is inside a magnetic field coincident with a temperature gradient a pressure gradient is generated in the magnetic fluid [5]. As the fluid increases its temperature its magnetization decreases and it is displaced by the cooler fluid with higher magnetization. The result is fluid propulsion with no moving mechanical parts.

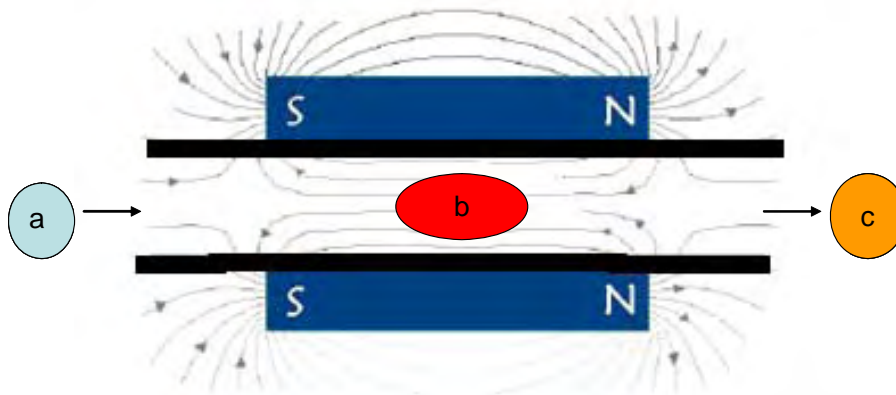


Figure 14. Scheme of a magnetocaloric pumping system. The letter *a* represent the zone were the cool magnetic fluid will enter, *b* is the heating zone and *c* the exit zone of the magnetic fluid at higher temperature

However, if the Curie temperature is far above the operational temperature of the system, the change in magnetization would be negligible. Most commercial grade magnetic fluids use magnetite nanoparticles and their Curie temperature is approximately 585 °C [5], too high for applications at operational temperatures near the room temperature at which many thermal systems work; so it is of great importance to the present investigation to obtain a ferrofluid with a Curie temperature near to 100 °C.

1.5.3 Related works on synthesis and magnetocaloric applications of ferrites

Jeyadevan *et al.* reported a growth-assisted co-precipitation process to achieve highly magnetic Mn–Zn ferrite particles. The ferrite composition was $(\text{MnO})_{0.41}(\text{ZnO})_{0.18}(\text{Fe}_2\text{O}_3)_{0.41}$. In this method, first, the particles were synthesized by co-precipitation under optimum conditions like 1h reaction time, 500rpm for the mechanical stirring and the corresponding concentration of the reactant. Then, further enhancement in particle size was obtained by using the already prepared particles as seeds. They succeeded in synthesizing Mn–Zn ferrite with a larger average diameter by growing the Mn–Zn ferrite seeds used to induce heterogeneous nucleation. As a result, the average particle diameter and magnetization of the particles increased from 9nm to 12nm and 37emu/g to 50emu/g, respectively. The higher magnetization resulted in a higher magnetization temperature gradient and could serve as a potential candidate for preparation of temperature sensitive magnetic fluid [7].

In the temperature sensitive of magnetic fluid Parekh *et al.* talk about how the pyromagnetic coefficient for three different fluid changing are function of the physical and magnetic properties such as size, magnetization and Curie temperature. Also, they developed a theoretical model to explain the behavior in entropy as a function of temperature.

For this purpose, they used $Mn_{0.5}Zn_{0.5}Fe_2O_4$, $Fe_{0.5}Zn_{0.5}Fe_2O_4$ and $Fe_{0.3}Zn_{0.7}Fe_2O_4$ ferrites. The following table summarizes the results:

Code	M_d (emu/cc)	D_m Å	T_c (K)
$Mn_{0.5}Zn_{0.5}Fe_2O_4$	210	71	340
$Fe_{0.5}Zn_{0.5}Fe_2O_4$	200	57	364
$Fe_{0.3}Zn_{0.7}Fe_2O_4$	100	43	347

Tabla 3. Magnetic properties of prepared magnetic fluid [19]

R. Arulmurugan et al. focused on the study on thermal-magnetic properties of Mn-Zn ferrite nanoparticles in a ferrofluid. They prepared ferrite nanoparticles by chemical co-precipitation for the magneto-thermal fluid. Precipitated particles were used for ferrofluid preparation. The fine particles were suitably dispersed in heptane using oleic acid as the surfactant. $Mn_{1-x}Zn_xFe_2O_4$ (with x varying from 0.1 to 0.5) were synthesized. The following table shows the variation in the magnetization value of $Mn_{1-x}Zn_xFe_2O_4$ with the atomic fraction of Zn, 'x'.

$Mn_{1-x}Zn_xFe_2O_4$	M_s (emu/g)
0.1	44
0.2	50
0.3	48
0.4	38
0.5	35

Tabla 4. Variation of magnetization in $Mn_{1-x}Zn_xFe_2O_4$ [20]

The Curie temperature and the specific magnetization decreased with the increase in zinc substitution from 0.1 to 0.5 [20].

R.V. Upadhyay et al. in 1999, he studied the physical and magnetic properties of Gd-substituted ferrite ferrofluid. This fluid has a Curie temperature of 348 K. The study indicated the possibility of enhancing the pyromagnetic coefficient of the magnetic fluid using Gd. The Curie temperature of Gd substituted ferrite ferrofluid increased slightly (348 K) compared to that of pure Mn-Zn ferrite ferrofluid (340 K) [21].

Another work on the rare-earth substitution of Mn-Zn ferrites is the one reported by N. Brusentsova et al. Gd-substituted Mn-Zn ferrite nanoparticles of different compositions were synthesized by chemical coprecipitation method. To study the reduction of the Curie temperature (T_C) for different samples, their magnetic properties in dependence from the composition and cationic distribution were investigated. An attempt to lower the T_C of superparamagnetic particles to the optimal temperature required in magnetic fluid hyperthermia (44–47 °C) was made. Apparently, to this work, it is not possible to get the ferrites of this composition with the T_C lower than 70–100 °C. It was suggested the need of including additional components, such as Mg or Cu(II), and try to then substitute Fe(III) further to lower the T_C value [22].

R. Arulmurugan also investigated Co-Zn substituted ferrites of the type $\text{Co}_{1-x}\text{Zn}_x\text{Fe}_2\text{O}_4$ with x ranging from 0.1 to 0.5 and prepared by co-

precipitation. This preparation procedure favored the formation of complex Co-Zn substituted ferrite nanoparticles. The particles were characterized by XRD. The particle size was calculated by using the Scherrer's formula. The size of the particles precipitated was less than 12 nm. TG-DTA studies confirmed the presence of associated water content in the precipitated nanoparticles and indicated that ferritization was complete. The temperature dependent magnetization was recorded at two different fields (5 kOe and 1 kOe). The Curie temperature of the powders was calculated by extrapolating the linear part of the temperature-dependent magnetization data measured at 1 kOe. The thermo-magnetic coefficient which is the first derivative of the temperature-dependent magnetization curve helped to understand the redistribution of cations between A and B sites, taking place during the process of heating in the case of nanoparticles. The temperature at which cationic redistribution takes place depends on the zinc concentration. From the value of thermo-magnetic coefficient and the temperature range, it became clear that $\text{Co}_{0.5}\text{Zn}_{0.5}\text{Fe}_2\text{O}_4$ particles could be used for the preparation of temperature-sensitive ferrofluids [23, 24].

Sample composition	$D_{(311)}$ nm	M_s (emu/g)	M_r (emu/g)	H_c (Oe)	Estimate T_c (°C)
$Co_{0.90}Zn_{0.10}Fe_{1.96}O_4$	12.0	54.1	10.60	223.0	415
$Co_{0.81}Zn_{0.20}Fe_{1.98}O_4$	11.1	50.7	4.84	76.2	373
$Co_{0.70}Zn_{0.31}Fe_{1.96}O_4$	9.7	48.8	2.35	33.5	352
$Co_{0.61}Zn_{0.41}Fe_{1.96}O_4$	8.8	42.8	0.80	11.6	285
$Co_{0.51}Zn_{0.50}Fe_{1.95}O_4$	8.4	39.6	0.50	9.8	267

Tabla 5. Co-Zn ferrite composition and magnetic properties [23].

In order to study and understand the size control effect on the magnetic properties, R. Justin Joseyphus et al. synthesized 20nm-80nm $Mn_{0.67}Zn_{0.33}Fe_2O_4$ nanoparticles, using an oxidation method. It was demonstrated that the particle size can be tailored by varying the concentration of the oxidant. The magnetization of the 80nm particles was $49 \text{ A m}^2 \text{ kg}^{-1}$ compared to $34 \text{ A m}^2 \text{ kg}^{-1}$ for the 20nm particles. The Curie temperatures for all the samples are found to be within $630 \pm 5K$ suggesting that there is no size-dependent cation distribution. The critical particle size for the superparamagnetic limit was found to be about 25 nm. The effective magnetic anisotropy constant was experimentally determined to be 7.78 kJ m^{-3} for the 25nm particles, which is about an order of magnitude higher than that of the bulk ferrite [25].

The work of Jun Wang et al. helped us to understand how the distributions of the Fe^{+3} in the ferrite will change the magnetic

properties. $Zn_{1-x}Mn_xFe_2O_4$ nanoparticles were synthesized through a hydrothermal process at $180^\circ C$. X-ray diffraction (XRD) and transmission electron microscope (TEM) studies show an increase in particle size with the increasing of Mn concentration. The saturation magnetization (M_s) of $Zn_{1-x}Mn_xFe_2O_4$ measured in a vibrating sample magnetometer (VSM) increased rapidly at first and then slowly by increasing the Mn concentration. Mossbauer spectroscopy analyses revealed that the spectra change from a paramagnetic double peak to hyperfine magnetic sextets and the $Zn_{0.2}Mn_{0.8}Fe_2O_4$ nanoparticles have 43% inversion occupancy on the tetrahedral sites by Fe^{3+} cations, while this value increases to 47% in the $MnFe_2O_4$ sample. The results showed that the occupancy of cations on A and B sites affected magnetic properties of spinel ferrite nanoparticles [26].

B. Skołoszewska et al. used solid state reaction to prepare ferrite powders. The limitation of this method is the formation of micrometric particles. Synthesis of magnesium–zinc [$(Mg_{0.63}Zn_{0.37})(Mn_{0.1}Fe_{1.8})O_{3.85}$] and manganese–zinc [$(Mn_{0.55}Zn_{0.35}Fe_{0.1})Fe_2O_4$] ferrites by solid-state reaction method was described. Brunauer–Emmett–Teller (BET) surface areas of the ferrite powders used for synthesis were $2.63\text{ m}^2/\text{g}$ for Mg–Zn ferrite and $2.86\text{ m}^2/\text{g}$ for manganese–zinc ferrite, respectively. The dense sintered bodies of Mg–Zn and Mn–Zn ferrites obtained at ($1250\text{ }^\circ C$ – $1300\text{ }^\circ C$) were characterized by the presence of Fe_2O_3 particles

uniformly dispersed through a cross-section. The samples were distinguished by small core losses and small coercive forces characteristic for soft magnetic materials. The hysteresis loops width for powdered materials were of the order of 15–35 Oe, whereas for sintered specimens they were less than 1 Oe. The saturation magnetization for powders was different from that of sintered samples [27].

E. Ateia et al. studied the effect of rare earth doping in MnZn ferrite. Dielectric constant, AC conductivity, and Seebeck coefficient were measured for $Mn_{0.5}Zn_{0.5}RyFe_2O_4$; where R= Dy, Gd, Sm, Ce, or La. Ferrites were prepared by standard ceramic technique and sintered at 1200 °C with a heating rate 4 °C/min. X-ray diffractograms evidenced the spinel structure in all samples, with the appearance of small peaks representing secondary phases. There is a lowering in the porosity starting after Sm-doped samples due to the presence of the secondary phases, which limits the grain growth. Due to Seebeck measurements the Mn–Zn ferrite doped with the rare earth was classified as P-type semiconductors. It was possible to increase the electrical resistivity by using a small quantity of Dy^{3+} ions substitutions owing to the structural heterogeneity generated by the insulating intergranular layers [28].

Yimin Xuan et al. reported the synthesis of Mn–Zn ferrite nanoparticles ($Mn_{1-x}Zn_xFe_2O_4$) by a hydrothermal precipitation approach using metal sulfate solution and aqueous ammonia. The magnetic characterization of

the particles revealed a strong influence of the Zn atomic fraction 'x' on the magnetic properties of the solids. No effect on particle size was discussed nor analyzed [29].

Based on the above summarized literature review, our research was focused on, at first, evaluate the effect of chemical composition (variation in Mn atomic fraction and Gd atomic fraction) on the structural and magnetic properties of the ferrite nanocrystals. On that basis, we moved out to evaluate the effect of materials syntheses under size-controlled conditions. The goal was to, after selecting a proper chemical composition, enlarge crystal size in order to improve magnetization and, eventually, the pyromagnetic coefficient and the technical Curie temperature in our powders.

1.6 NUCLEATION AND GROWTH PROCESSES IN NANOSIZE CRYSTALS FORMATION

In liquid phase, uniform particles are usually prepared via homogeneous precipitation reactions, a process that involves the separation of the nucleation and growth of the nuclei. A schematic representation of the different mechanisms proposed to explain the formation of uniform particles is shown in the next Figure.

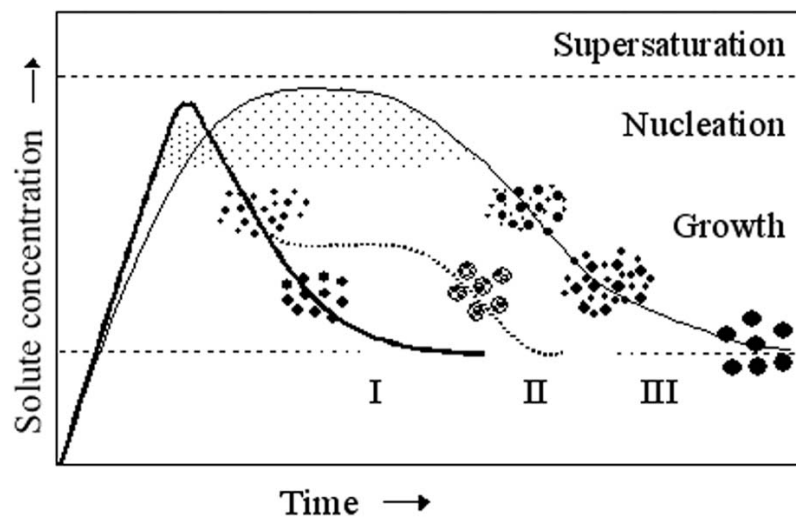


Figure 15. Classical model proposed by LaMer and Dinegar to explain the mechanism of formation of colloids [30]

In a homogeneous precipitation, a short single burst of nucleation occurs when the concentration of constituent species reaches critical supersaturation. Then, the nuclei so obtained are allowed to grow uniformly by diffusion of solutes from the solution to their surface until the final size is attained. To achieve monodispersity, these two stages

must be separated and nucleation should be avoided during the period of growth. This is the classical model proposed first by LaMer and Dinegar [30] to explain the mechanism of formation of sulfur colloids and also for a limited number of cases (curve I of Figure 1). However, uniform particles have also been obtained after multiple nucleation events. Some authors have explained the uniformity of the final product in this case through a self-sharpening growth process (Ostwald ripening, curve III of Figure 1). Another mechanism proposes that uniform particles can also be obtained as a result of aggregation of much smaller subunits rather than continuous growth by diffusion (curve II of Figure 1). On the other hand, an artificial separation between nucleation and growth processes may be achieved by seeding, a process in which foreign particles are introduced into the solution of monomers below the critical supersaturation.

1.7 FUNDAMENTAL OF MATERIALS CHARACTERIZATION

1.7.1 X-Ray Diffraction (XRD)

The crystalline structures of various magnetic materials were investigated by Wide Angle X-Ray Diffraction (WAXD), using a powder X-Ray diffractometer (Siemens D 500 model) with Cu-K α source and β -Ni filter (Figure 16). All the scans were recorded in the 2θ regions of 15

- 75° at a scan rate of 0.02° per second.



Figure 16. XRD Siemens D500 unit at the Department of Engineering Science and Materials UPRM.

X-ray Diffraction (XRD) is a powerful technique used to uniquely identify the crystalline phases present in materials and to measure the structural properties (strain state, grain size, epitaxy, phase composition, preferred orientation, and defect structure) of these phases. XRD is also used to determine the thickness of thin films and multilayers, and atomic arrangements in amorphous materials (including polymers) and at interfaces. Figure 17 shows the basic features of an XRD experiment set up, the diffraction angle 2θ is the angle between the incident and diffracted X rays [31-32]. From 2θ values for reflection, 'd' values were

calculated using Bragg equation and average crystallite size calculated of ferrite nanoparticles by Scherrer's equation.

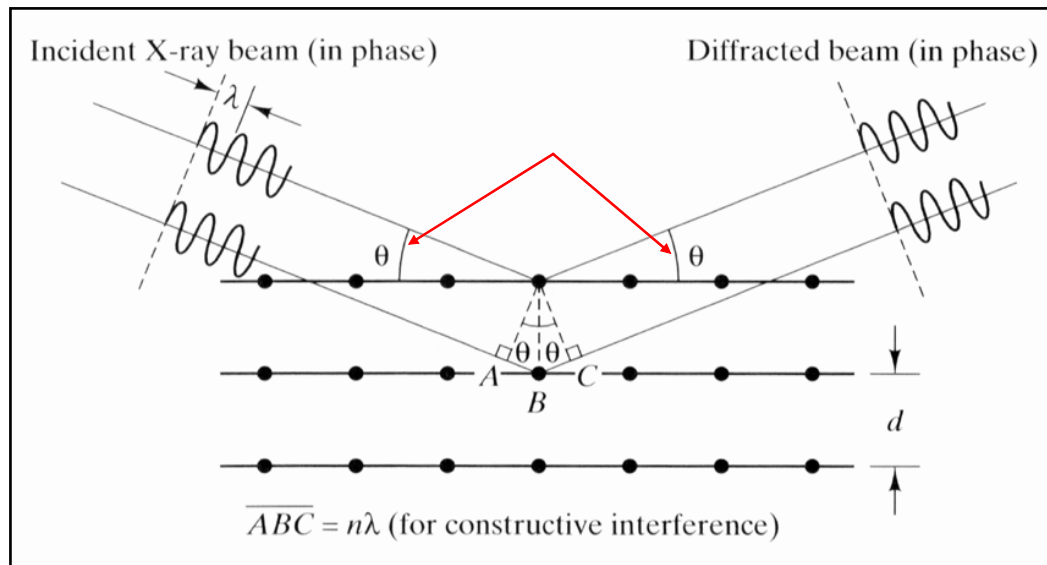


Figure 17. Basic features of a typical XRD experiment.

Crystals consist of planes of atoms that are spaced a distance d apart (Figures 18 and 19), but can be resolved into many atomic planes, each with a different d -spacing. For the familiar cubic crystal, these form an orthogonal system. Any atomic plane can now be uniquely distinguished by its Miller indices. These are the three reciprocal intercepts of the plane with the a -, b -, and c -axes and are reduced to the smallest integers having the same ratio. The d -spacing between (hkl) planes is denoted d_{hkl} , and for cubic crystals, it is where a is the lattice constant of the crystal (see Figure 20)

$$d_{hkl} = \frac{a_0}{\sqrt{h^2 + k^2 + l^2}} \quad \text{Equation (8)}$$

when there is constructive interference from X rays scattered by the atomic planes in a crystal, a diffraction peak is observed. The condition for constructive interference from planes with spacing d_{hkl} is given by Bragg's law:

$$\lambda = (2)(d_{hkl})(\sin\theta_{hkl}) \quad \text{Equation (9)}$$

where θ_{hkl} is the angle between the atomic planes and the incident (and diffracted) X-ray beam (Figure 17). For diffraction to be observed, the detector must be positioned so that the diffraction angle is $2\theta_{hkl}$, and the crystal must be oriented so that the normal to the diffracting plane is coplanar with the incident and diffracted. Figure 18 shows several atomic planes and their d-spacing in a simple cubic (sc) crystal

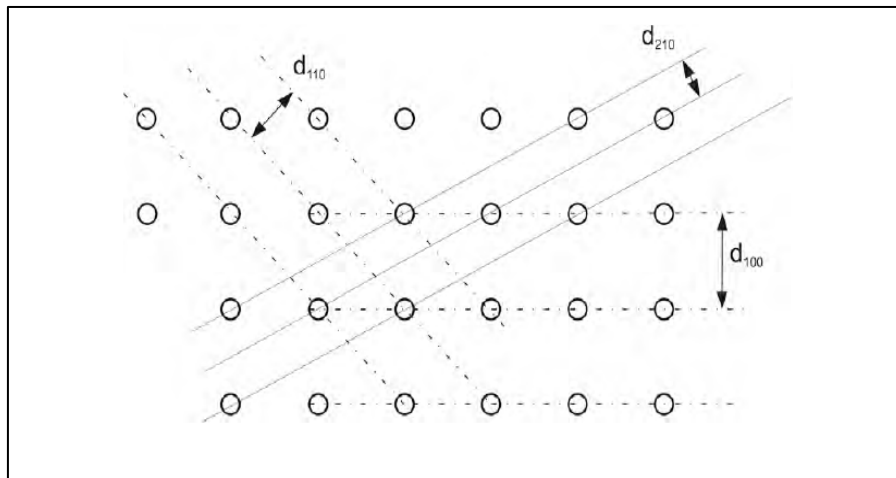


Figure 18. Atomic planes and their d-spacings in a simple cubic (SC) unit cell.

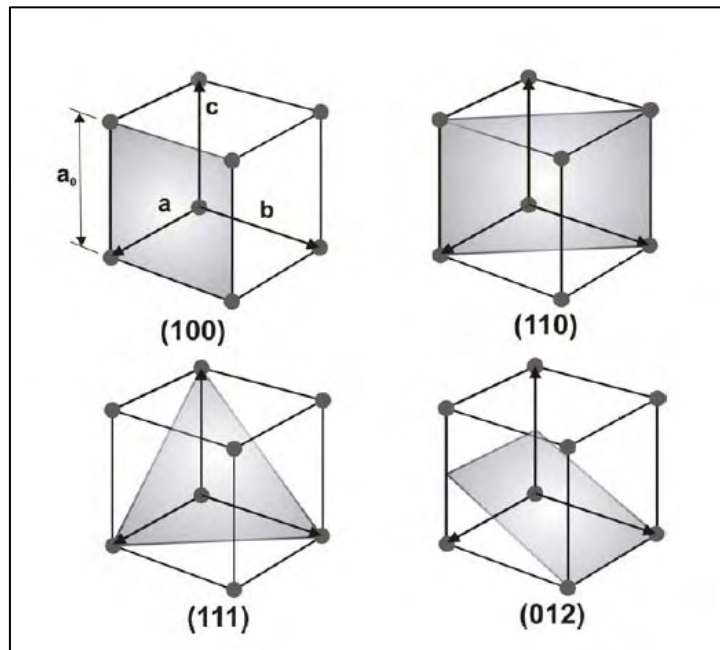


Figure 19. Miller indices of atomic planes in a SC unit cell.

1.7.2 Transmission Electron Microscopy (TEM)

For the evaluation of the ferrite dispersion, a 200 kV high resolution Philips CM200 ULTRA TWIN TEM (Figure 20) with 0.19 point resolution, Ge light element energy-dispersive x-ray spectroscopy (EDS), and full image processing and analysis capabilities were used. This equipment belongs to Materials Science Center in University of Wisconsin.



Figure 20. TEM Philips CM200 UT CM200 UT at the Department of Materials Science & Engineering, University of Wisconsin.

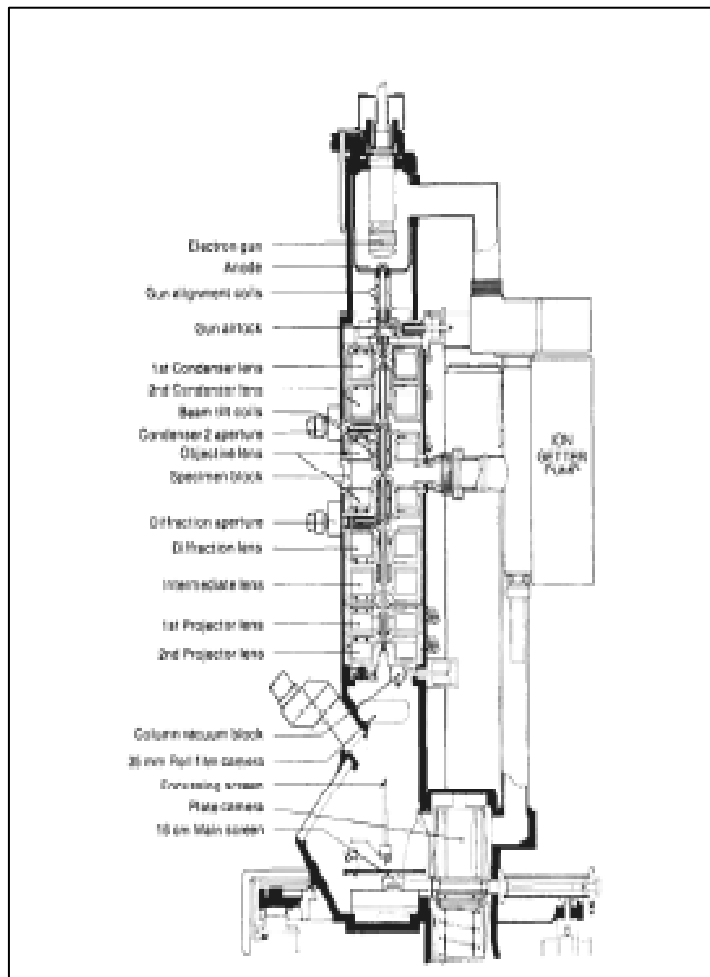


Figure 21. Schematic diagram of a TEM instrument, showing the location of a thin sample and the principal lenses within a TEM column [36].

TEM's strong cards are its high lateral spatial resolution (better than 0.2 nm "point-to point" on some instruments) and its capability to provide both image and diffraction information from a single sample. In addition, the highly energetic beam of electrons used in TEM interacts with sample matter to produce characteristic radiation and particles; these signals are often measured to provide materials characterization using EDS, EELS, EXELFS, backscattered and secondary electron imaging, to

name a few possible techniques.

A "light source" at the top of the microscope emits the electrons that travel through vacuum in the column of the microscope. Instead of glass lenses focusing the light in the light microscope, the TEM uses electromagnetic lenses to focus the electrons into a very thin beam. The electron beam then travels through the specimen you want to study. Depending on the density of the material present, some of the electrons are scattered and disappear from the beam. At the bottom of the microscope the unscattered electrons hit a fluorescent screen, which gives rise to a "shadow image" of the specimen with its different parts displayed in varied darkness according to their density. The image can be studied directly by the operator or photographed with a camera.

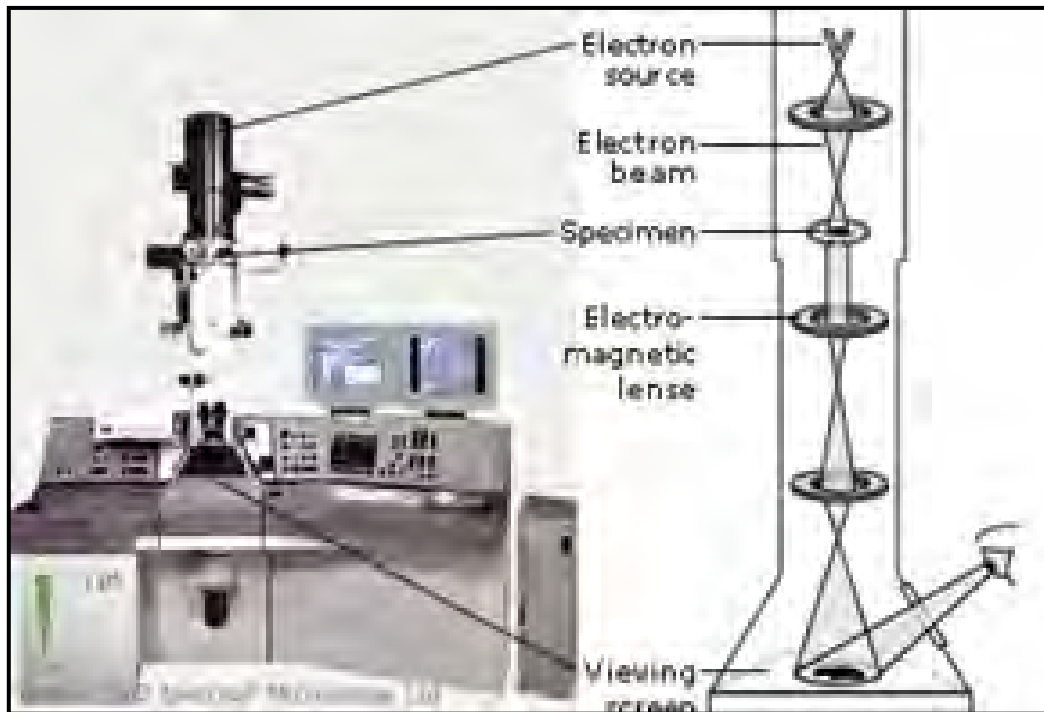


Figure 22. Schematic representation for the ray paths of both unscattered and scattered electrons beneath the sample.

1.7.3 Vibrating Sample Magnetometer (VSM)



Figure 23. Lake Shore 7400 Series VSM at the Department of Engineering Science & Materials at UPRM.

In order to obtain a measurement of the magnetic induction it is also possible to use an instrument with various moving-coils. The simplest of these is the rotating coil which rotates at a fixed angular velocity. Therefore the amplitude of the generated voltage by rotating coil is proportional to the magnetic induction and therefore the amplitude can be used to measure magnetic induction (B) or magnetic field (H) in free space. The signal can be read directly as an AC voltage or converted to a DC voltage which is proportional to the amplitude [31].

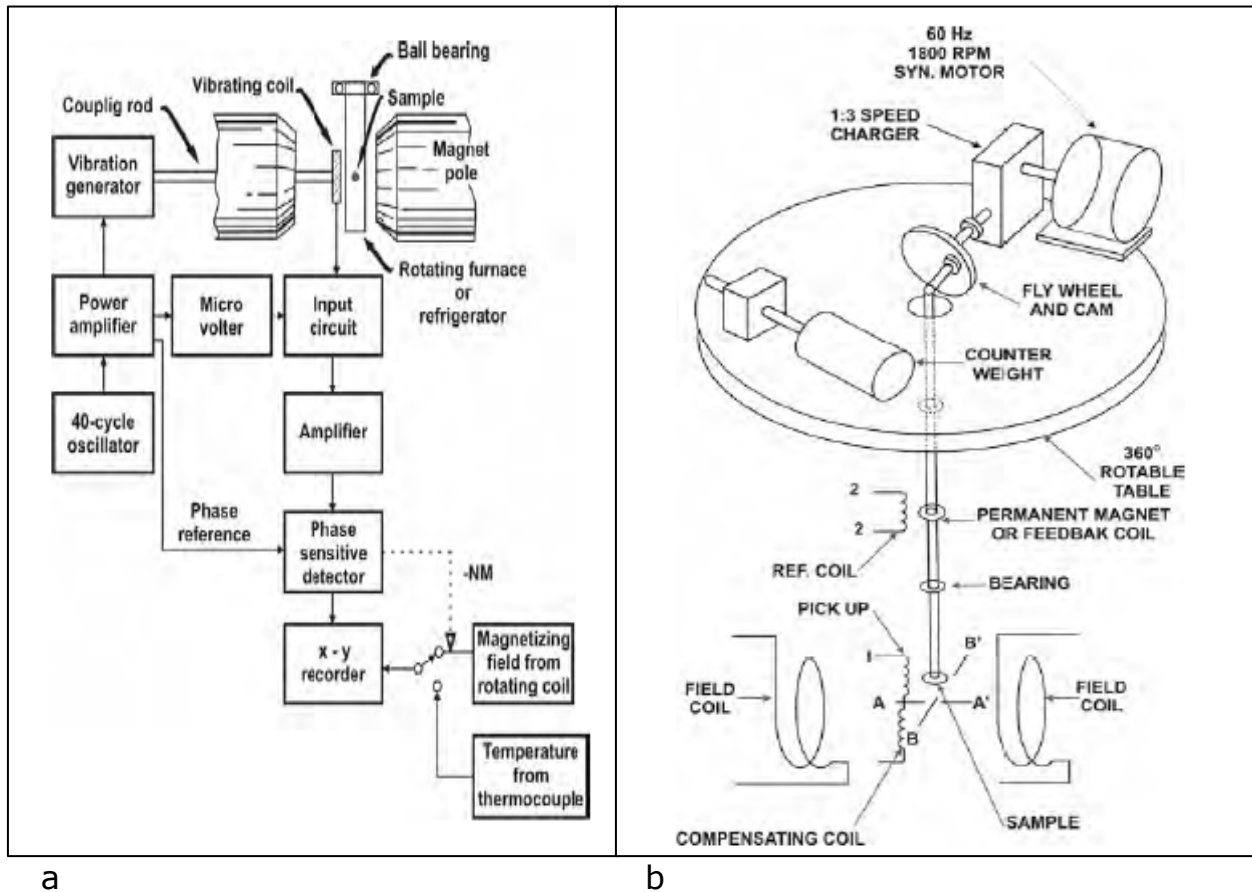


Figure 24. (a) Schematic diagram of a vibrating coil magnetometer and (b) schematic diagram of a vibrating sample magnetometer.

A VSM is really a gradiometer measuring the difference in magnetic induction between a region of space with and without the specimen. It therefore gives a direct measure of the magnetization. A schematic of a typical VSM is shown in Figure 24 (b). The specimen in general has to be rather short to fit between poles of the electromagnet. The method is therefore in most cases not well suited to the determination of the magnetization curve or hysteresis loop because of the demagnetizing effects associated with the short specimen. However it is well suited for the determination of the saturation magnetization (M_s).

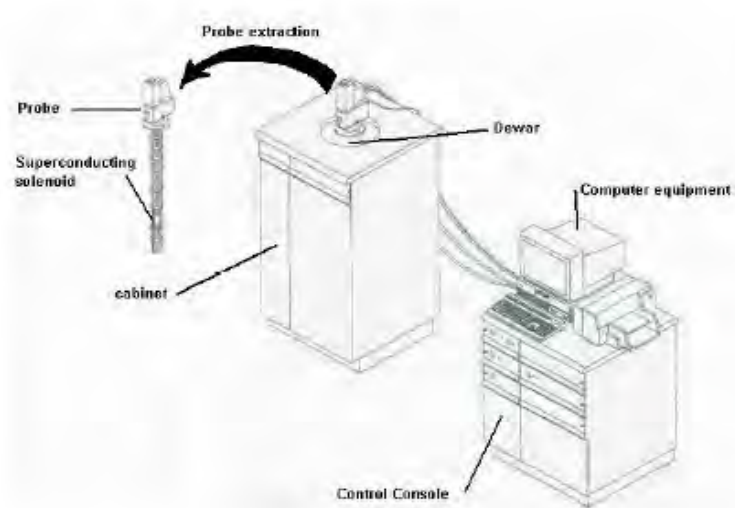
The detected signal, being an AC signal of fixed frequency, is measured using a lock-in amplifier. A reference signal is provided for the lock-in amplifier as shown in Figure 24 by using a permanent magnet and a reference pick-up coil. Magnetic moments as small as 5×10^{-4} A m² (5×10^{-5} emu) are measurable with a VSM. Its accuracy is better than 2% [33].

1.7.4 Superconducting Quantum Interference Devices (SQUID)

A Quantum Design XL-7 Magnetic Properties Measurement System (MPMS), with a superconducting quantum interference device (SQUID) detector, provides the ultimate in resolution for magnetic measurements [34]. The SQUID unit can work in the temperature range between 1.9 and 400 K and under a maximum applied field of 7 T. The heart of the MPMS is the superconducting detection coil. The detection coil is located at the midpoint of the superconducting solenoid, which is used to create the applied field. The SQUID sensitivity is usually of the order of 10^{-8} emu with an accuracy of 1%, which is more sensitive than other magnetometers like Vibrating-sample Magnetometer (VSM), 5×10^{-5} emu. This high sensitivity makes the SQUID a perfect choice to measure small magnetic signals.



a



b

Figure 25. (a) Quantum Design MPMSXL available at UPRM and (b) schematic diagram of the SQUID unit.

SQUID measures the magnetic moment by moving the sample through the detection coil. The magnetic moment of the sample creates a flux in the detection coil, which changes with the sample position. The flux is converted to a voltage by the magnetometer and the voltage versus sample position data is further used to extract the magnetic moment. The software package supplied with the MPMS analyzes the voltage versus sample position data and determines a value for the magnetic moment as a result of a fitting procedure between a theoretically expected curve and the experimental data.

METHODOLOGY

1.8 MATERIALS

All reagents were of analytical grade and were used without further purification. Required weights of chloride salts of Fe(III), Zn(II), Mn(II), Gd(III) and Eu(III) ions were dissolved in distilled water to achieve a (Fe+Gd or Eu)/M, (M = Mn+Zn), mole ratio of two. NaOH was used as the alkaline precipitant agent.

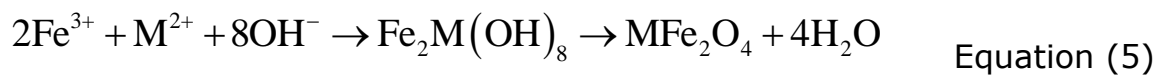
1.9 EXPERIMENTAL

The synthesis of Mn-Zn ferrite was carried out by the co-precipitation method. The conventional approach was modified by controlling the flow-rate at which the reactants are mixed together. The purpose of this control was to evaluate the possibility of promoting heterogeneous nucleation and hence, crystal growth. The control on the crystal size will permit the improvement on magnetization of the particles.

The conventional co-precipitation method was used in the synthesis of the material; a solution containing 0.11 M Fe (III) and Gd(III) and 0.055M Mn(II) and Zn(II) ions at suitable amounts as required in $Mn_xZn_{1-x}RE_yFe_{1-y}O_4$ stoichiometry (RE= Gd), is contacted with a hot 0.48 M NaOH solution under boiling conditions and mechanically stirred at

500 rpm). The hydrolysis reaction produced the formation of a mixed paramagnetic Fe-M hydroxide, which undergoes de-hydration and atomic re-arrangement conducive to stoichiometric ferrite structure with no need of further annealing. From now and on, 'x' and 'y' will represent the atomic fraction of Mn(II) and Gd(III) or Eu(III) species, respectively (where 'M' is divalent metal cation).

The ferrite formation takes place according to:



The nucleation rate has been quite observed to be high at the beginning of the precipitation process whereas the excess of OH⁻ ions provides a net negative surface charge to the nuclei limiting their further growth and aggregation. Under these conditions polydisperse particles of less than 50nm in diameter are typically produced.

Size-controlled synthesis approaches are based on the promotion of heterogeneous nucleation, which in turn favor the growth of the nanocrystals. This control was achieved by a fine tuning of the addition flow-rate of the reactants.

Figure 26 summarizes the experimental procedure to synthesized Mn-Zn ferrite.

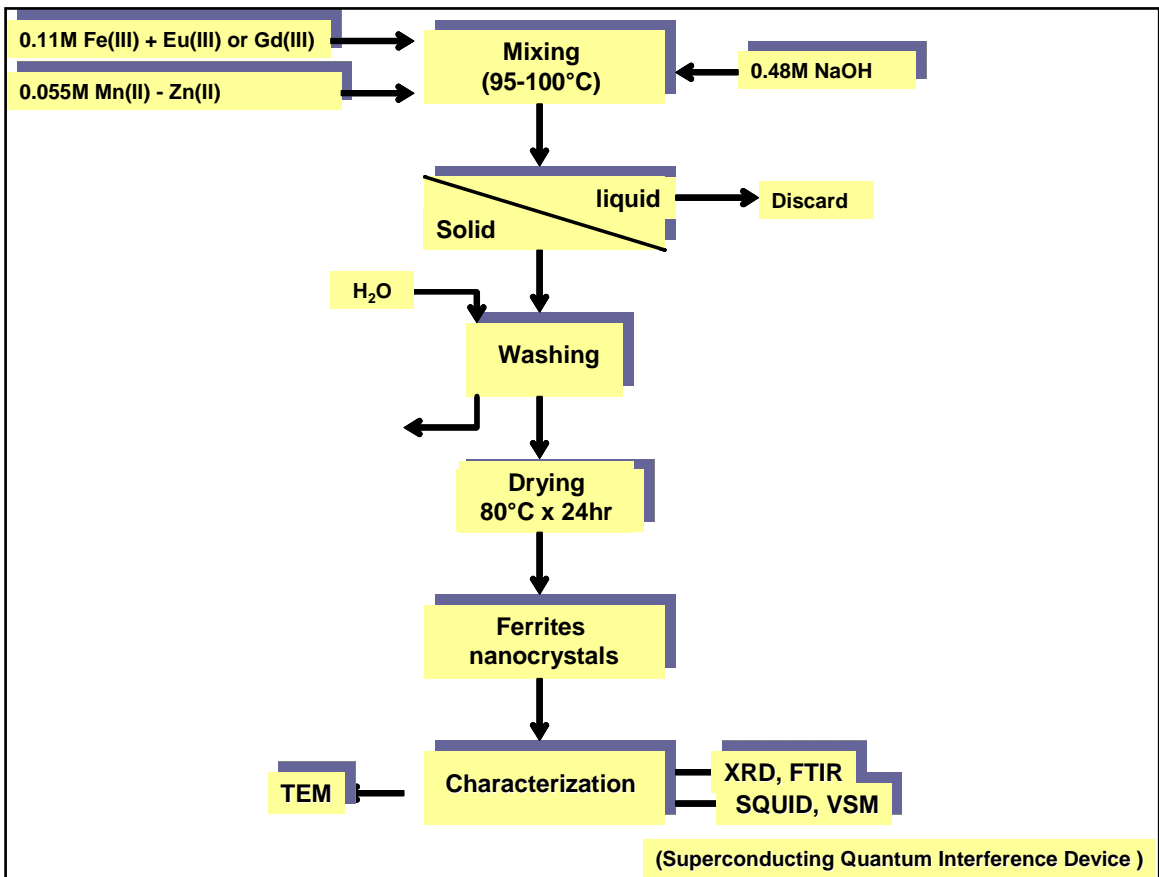


Figure 26. Experimental procedure for the synthesis of Mn-Zn ferrite nanocrystals.

1.10 CHARACTERIZATION.

Structural analysis of the powders were carried out in a Siemens D5000 x-ray diffractometer (XRD) using the Cu-K α radiation. The particle morphology was examined by high-resolution transmission electron microscope (HRTEM). Magnetic properties of powders were measured in Quantum Design SQUID and Lake Shore VSM magnetometers. M-T curves were obtained under an external magnetic field of 7 Tesla and 2.2 Tesla for SQUID and VSM, respectively. For the present work, we will use a 'Technical Curie temperature' that will be defined as the temperature at which the magnetization of compacted ferrite nanocrystals will be zero under the influence of a fixed external magnetic field (2.2 T in VSM and 7 T in a SQUID magnetometer). The effect of inter-particle magnetic interactions (as required when dealing with actual Curie temperature values in bulk magnetic materials) will not be considered under this practical definition.

The measurements of selected samples were repeated four times ($n=4$) in each one of the equipments mentioned above in order to determine the standard deviations within measurements. For XRD the standard deviation of the average crystal size was estimated at 0.001nm. It was 0.002nm for the lattice parameter. The standard deviation for the magnetization values was calculated at 1emu/g.

RESULTS AND DISCUSSION

1.11 MN-ZN FERRITE NANOCRYSTALS

1.11.1 Conventional co-precipitation synthesis of $Mn_xZn_{1-x}Fe_2O_4$

1.11.1.1 XRD Measurements

Figure 27 shows the XRD patterns for $Mn_xZn_{1-x}Fe_2O_4$ ferrites powders produced after 4 hours of reaction time and various atomic fractions of Mn ions ('x'). All reflections correspond to the ferrite structure; the structure, also known as spinel, is Face Centered Cubic. The relative intensities and angular positions of those peaks evidence the formation of this material for the whole range of Mn compositions considered. However, as the broadening in the XRD peaks at lower 'x' values suggests, the crystallinity i.e, average crystallite size, have decreased when the ferrite contained less amount of Mn ions.

The average crystallite size, estimated by using the Debye-Scherrer's equation for the (311) peak, ranged from 6nm to 15 nm when 'x' varied from 0 (zinc-ferrite) to 1.0 (manganese-ferrite). Table 6 summarizes the variation in average crystallite size and the ferrite lattice parameter as a function of the atomic fraction of Mn ions in the ferrite. It was observed that, a large proportion of zinc ions not only make the average crystal size to decrease but affects the solids crystallinity, as suggested by the

noise in the XRD signal for the corresponding solids. As was proposed before, the formation of the ferrite involves the dissolution of an intermediate (mixed hydroxide); the faster this intermediate gets dissolved, the faster the development of the ferrite structure.

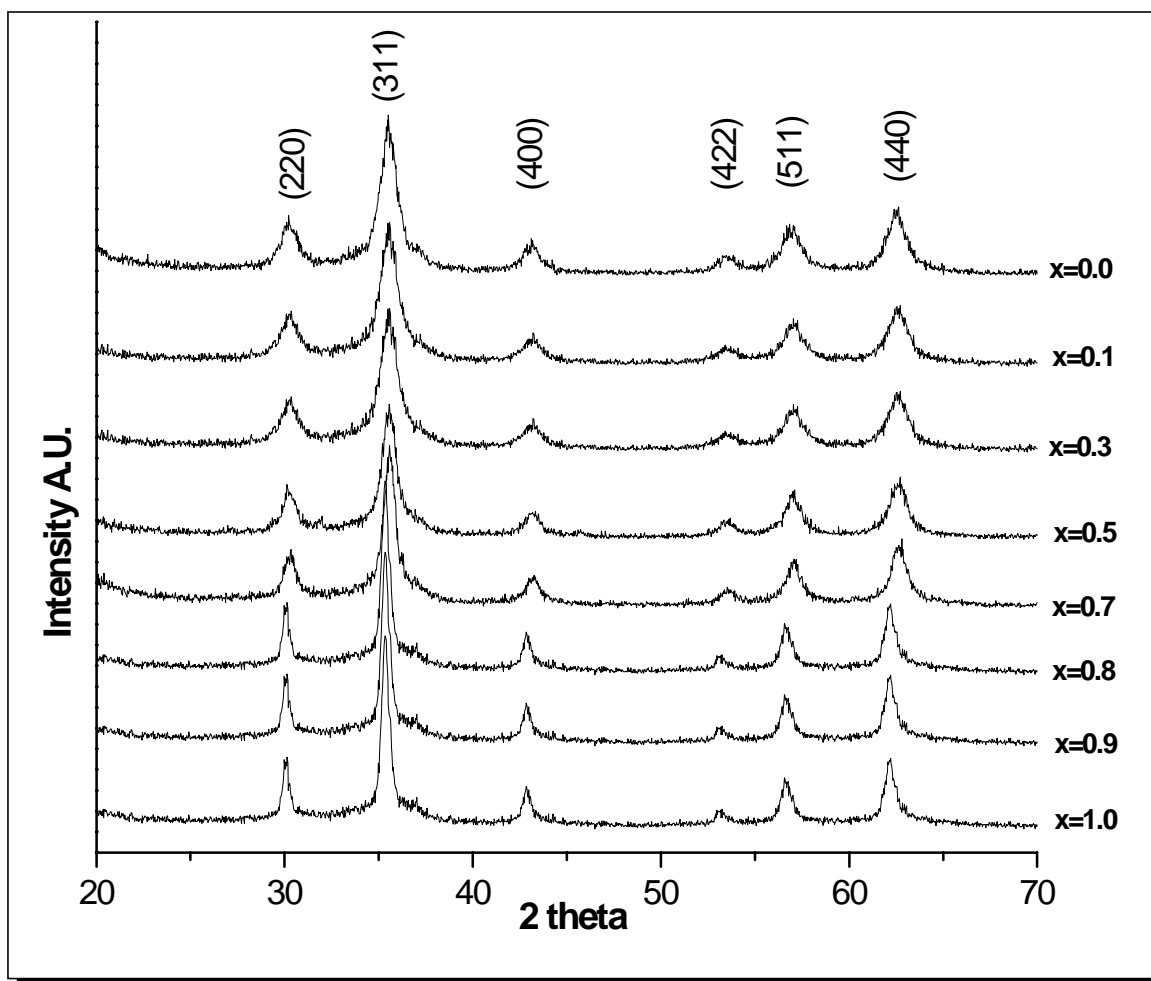


Figure 27. XRD patterns for Mn-Zn ferrites synthesized on a hot plate at different Mn atomic fraction 'x'.

x	Average Crystallite size +/-0.1(nm)	Lattice Parameter +/-0.002 (nm)
0	8.5	0.829
0.1	7.6	0.822
0.3	8.3	0.823
0.5	10.1	0.823
0.7	11.6	0.822
0.8	10.9	0.821
0.9	12.2	0.823
1.0	16.0	0.827

Tabla 6. Variation in average crystallite as a function of the atomic fraction of Mn ions in the $Mn_xZn_{1-x}Fe_2O_4$ ferrite.

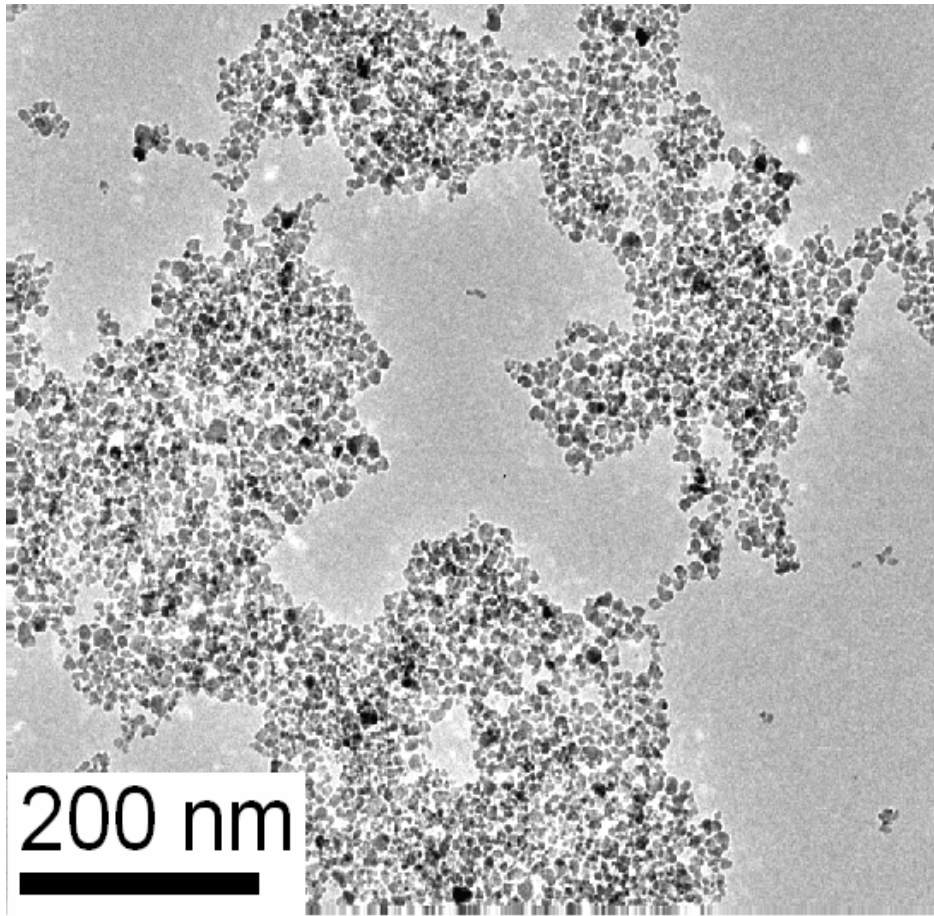
Although the rate of the re-dissolution step had been favored by the excess of NaOH during synthesis, those intermediates produced at larger fractions of Zn Ions (i.e, lower 'x' values) could have been less soluble under alkaline conditions. If the dissolution of this Zn-rich intermediate is inhibited, we should expect the inhibition on the formation of the ferrite structure and the corresponding growth of the ferrite nuclei. Using the best knowledge this is the first complete study on this type of ferrite, the variation in the average crystallite sizes of the particle as function of the fraction of Mn in the ferrite.

The lattice parameter did not exhibit any significant change with the ferrite composition. This value was $8.21 \text{ \AA} \pm 0.02 \text{ \AA}$, which is good

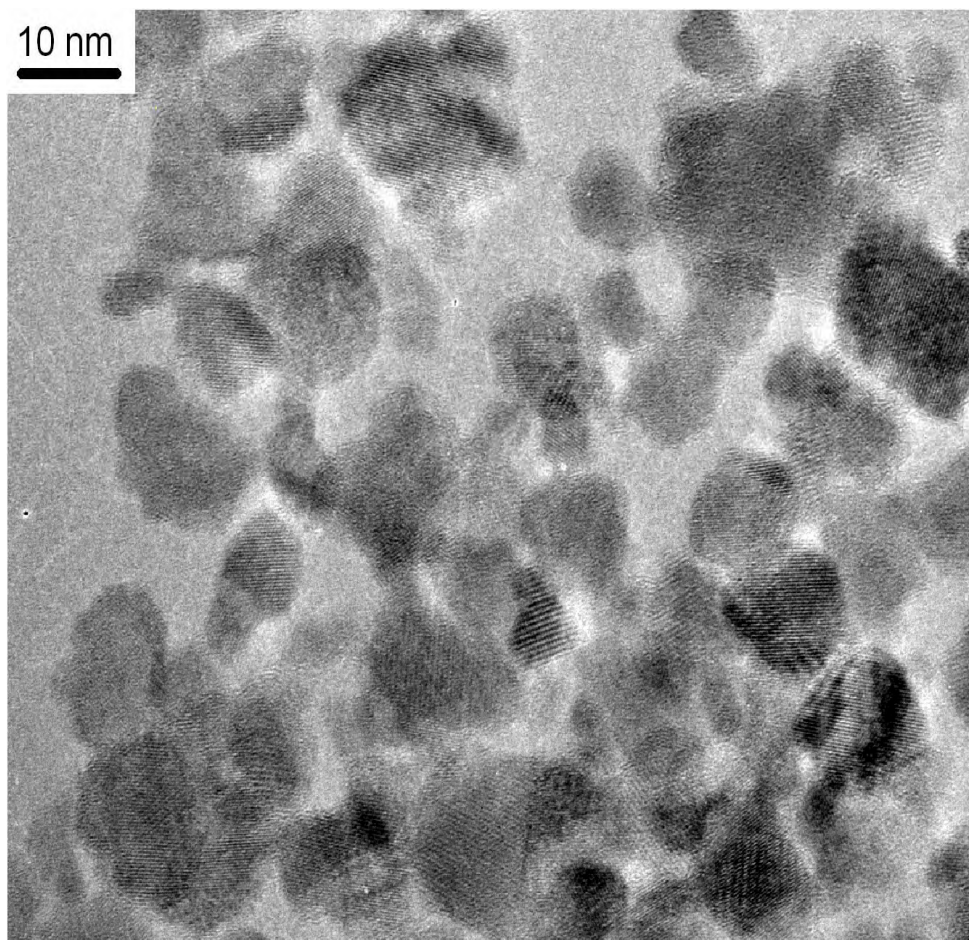
agreement with the bulk value of 8.31 Å for atomic fraction of Mn equal to 0.8. These results represent no different between the material in the micro scale and the nano scale; no change in the unit cell of the spinel structure has been evidence. The difference in the ionic radii between the Mn⁺² (0.83 Å) and Zn⁺² (0.73 Å) did not affect the formation of the structure. The substitution between Mn and Zn and the re-distribution in the A and B site was not affected in the evaluated range.

1.11.1.2 HRTEM observations

HRTEM images of figure 28 ('a' and 'b') evidence the nanocrystalline nature of the Mn-Zn ferrite particles, synthesized for 'x'=0.7. The observed particle size (~10 nm) is in good agreement with the value estimated from XRD analysis, which suggests the formation of single ferrite crystals. Moreover, some individual shows the lattice fringes, evidencing the high crystallinity of the products even at the nanoscale.



a



b

Figure 28. HRTEM images of $\text{Mn}_{0.7}\text{Zn}_{0.3}\text{Fe}_2\text{O}_4$ nanocrystals at different magnifications.

1.11.1.3 Magnetic Characterization

i. M-H measurements

Figure 29 shows the room temperature M-H curve for $\text{Mn}_x\text{Zn}_{1-x}\text{Fe}_2\text{O}_4$ nanocrystals synthesized at different Mn atomic fraction, 'x'. As seen, the degree of magnetic saturation and the corresponding magnetization

values were strongly dependent on the composition of the ferrites in the range evaluated. In general, our results are in good agreement with those reported by other researchers [4,7]. On the consideration that observed trends are exclusively related to compositions (i.e., no crystal size effects) the following interpretation can be proposed. In Mn-Zn ferrites divalent and Fe^{3+} ions occupy both A- and B-sites in the ferrite structure, with Zn^{2+} preferring A-sites. The incorporation of magnetic Mn^{2+} replacing non-magnetic Zn^{2+} ions could be related to the enhancement in the maximum magnetization with a rising 'x' value. For minor proportions of Mn^{2+} ions, i.e. low 'x' values, the ferrite would become a normal ferrite, i. e., no more Mn^{2+} in B-sites and no more Fe^{3+} in A-sites. The corresponding drop in magnetization can be related to this atomic redistribution. In absence of Mn substitution ('x'= 0) a compensated anti-ferromagnetic behavior is expected to be established in ZnFe_2O_4 . Nevertheless, Figure 3 shows that even for $x = 0$ and 0.1, produced ferrites exhibited a small magnetization. This small magnetization could be due to some inversion degree in the normal ZnFe_2O_4 ferrite structure where a small part of Zn^{2+} may still remain in B-sites and a part of Fe^{3+} in A-sites. The drop in magnetization observed for 'x' above 0.8, could be attributed to the decrease in A-B type interactions in the MnFe_2O_4 structure ('x'= 1.0) in comparison with those interactions in the $\text{Mn}_x\text{Zn}_{1-x}\text{Fe}_2\text{O}_4$ one.

Although the above presented discussion was based on the consideration of the variation in chemical composition only, the variation in the average crystallite size with the atomic fraction of Mn, showed in the previous discussion, could also be involved with the rise in magnetization. It is a well accepted fact that the crystal growth would be conducive to an increase on the magnetization of that the material, on a common weight basis.

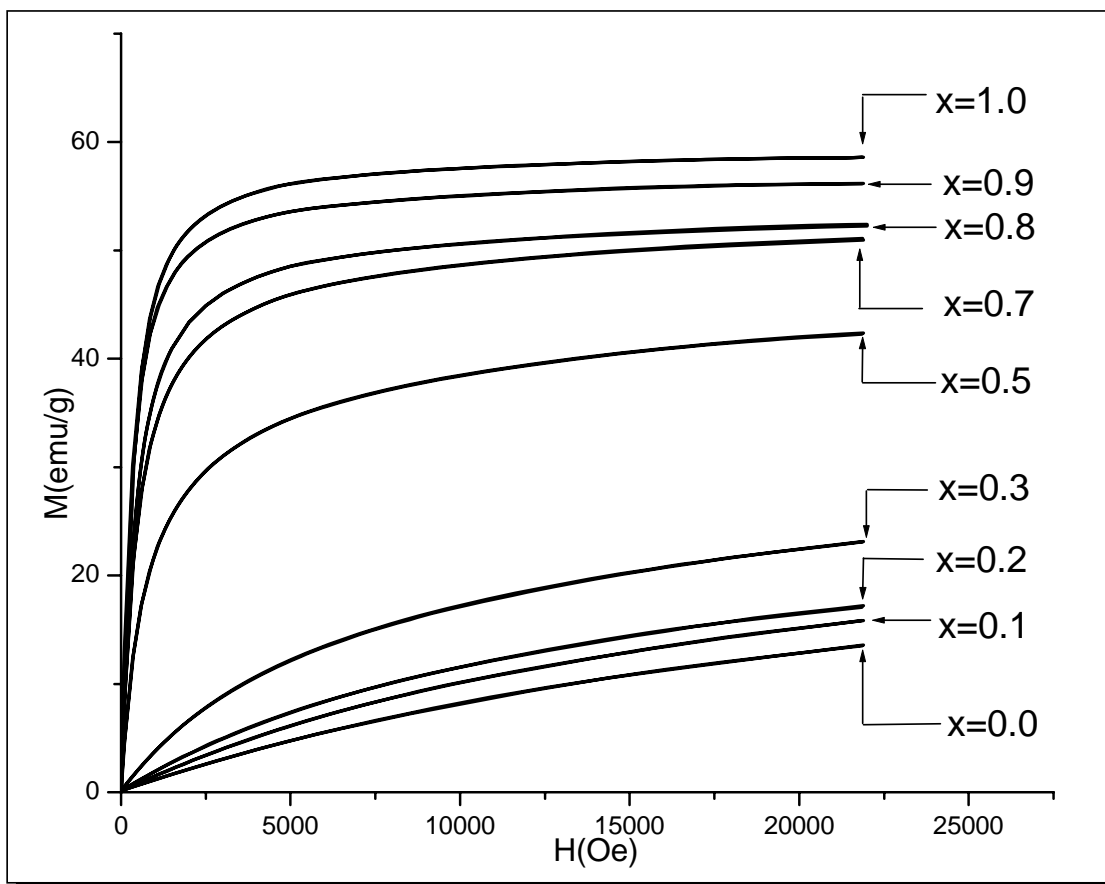


Figure 29. Room temperature M-H loops for $Mn_xZn_{1-x}Fe_2O_4$ ferrites synthesized at different Mn atomic fractions, 'x'.

The following Figure shows the variation in the maximum magnetization values and the average crystallite size as function of the atomic fraction of Mn ions, 'x'.

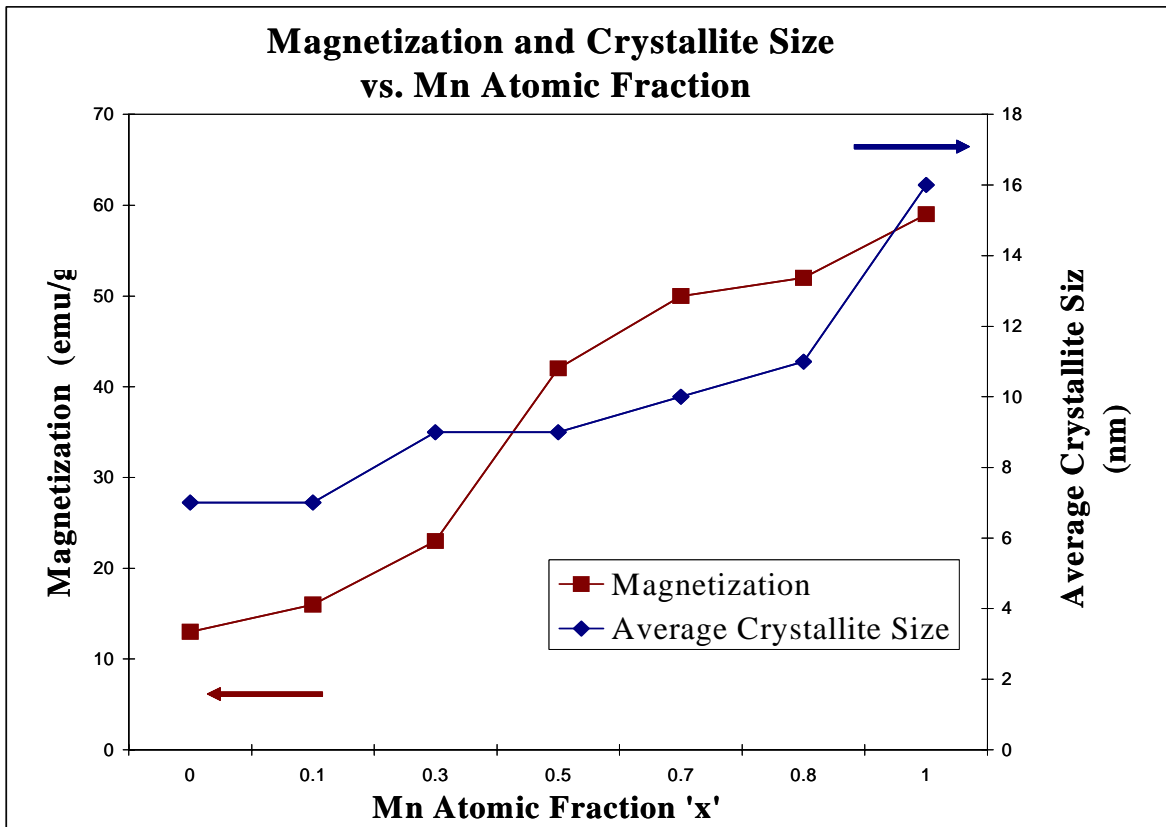


Figure 30. Magnetization and Average Crystallite size as a function of Mn atomic fraction.

Figure 29 also shows that even for $x = 0$ and 0.1 , produced ferrites exhibited a small magnetization. It could be due to some inversion degree in the $ZnFe_2O_4$ structure where a small part of Zn^{2+} may still remain in B-sites and a part of Fe^{3+} in A-sites. The drop in

magnetization observed for 'x' values above 0.8, could be attributed to the decrease in A-B type interactions in the MnFe_2O_4 structure ('x'= 1.0) in comparison with those interactions in the $\text{Mn}_x\text{Zn}_{1-x}\text{Fe}_2\text{O}_4$ one [4].

ii. M-T measurements

The variation in magnetization with temperature for ferrite nanocrystals synthesized at different 'x' values is summarized in figure 31. All measurements were carried out under an external magnetic field of 2.2 Tesla. As the figure shows, the higher the Mn atomic fraction in the ferrite, the higher the Curie Temperature (T_C). The incorporation of Mn^{2+} ions in the ferrite lattice, and the corresponding rearrangement of Fe(III) and Zn(II) species between A and B sites in the ferrite, should be involved with the observed trend. For some ferrites, containing copper and manganese an investigation was made of the influence of the modification of the cation distribution on the Curie point.

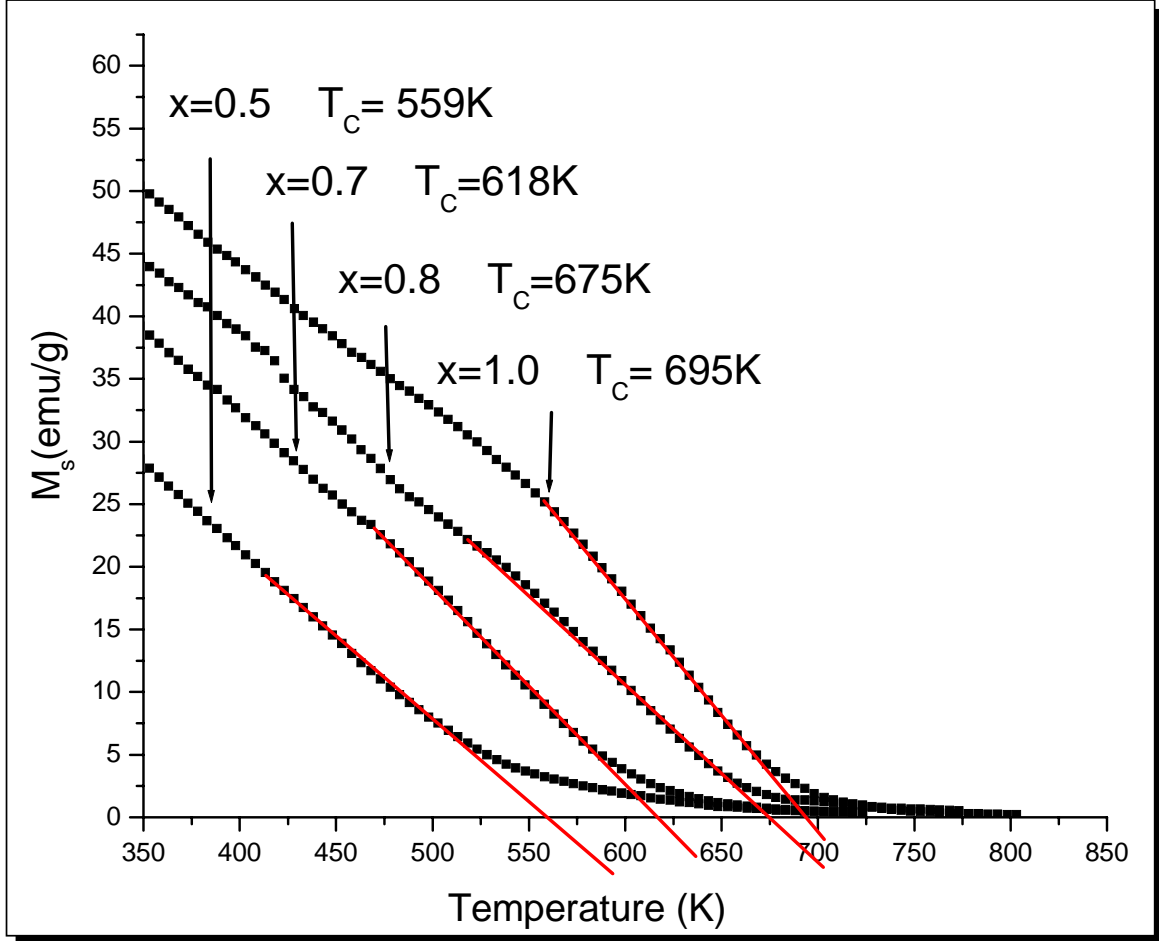


Figure 31. M-T plots for $Mn_xZn_{1-x}Fe_2O_4$ ferrites at different Mn atomic fractions, 'x'. The external magnetic field was 2.2 Tesla.

For the pure Mn-ferrite ($x=1.0$), the ferrites which contain manganese ions, the Curie point shift after oxygen treatment is less pronounced because of migration of manganese ions from octahedral to tetrahedral sites, which results in a shift of the Curie points to lower temperatures [35]. Our results disagreed with the trends observed for bulk materials because at nanoscale the T_C of the pure Mn ferrite is higher than the one

containing Mn and Zn. It has been reported that the increase in the amount of Mn in Mn-Zn ferrites, causes the rise in both, the magnetic moment of the unit cell and the T_C [36]. The increase of T_C value in case of Mn-Zn sample can be due to the increase of exchange interaction of AB and BB between octahedral and tetrahedral sites as proposed by Z.X.Tang, and C.M.Sorensen [37]. Figure 32 shows the technical Curie temperature values as function of the different Mn atomic fraction.

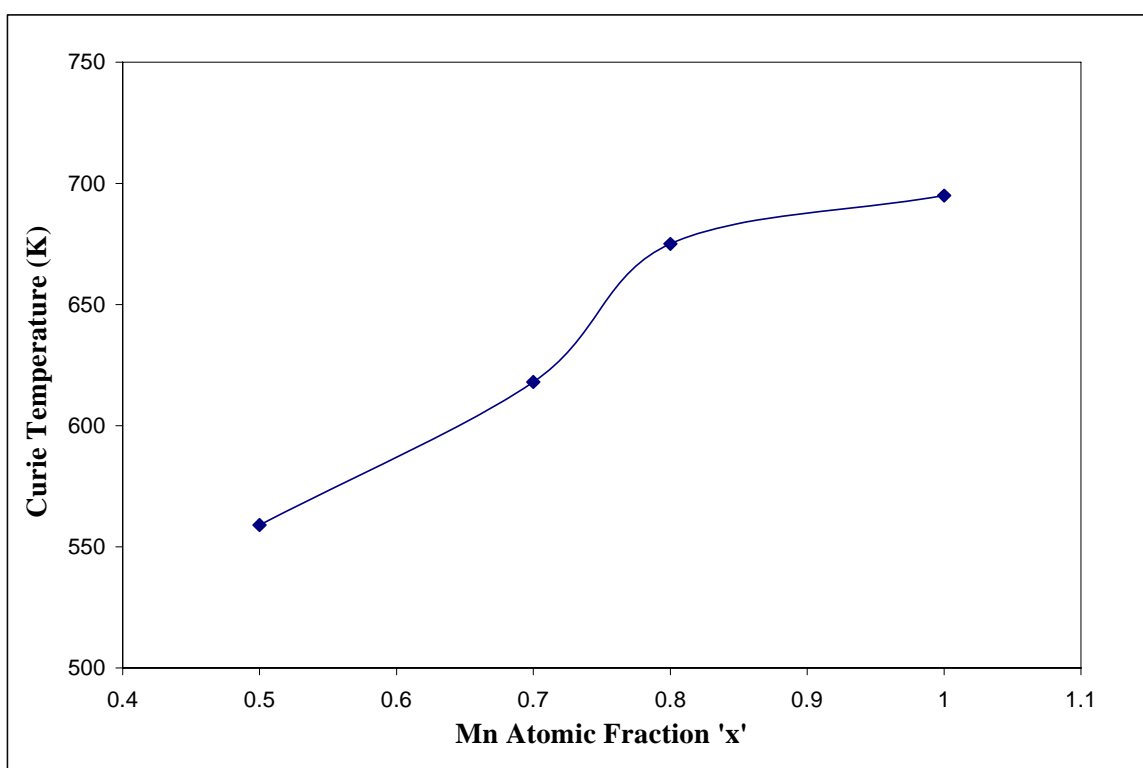


Figure 32. Variation of the technical Curie temperature with the Mn atomic fraction, 'x' in $Mn_xZn_{1-x}Fe_2O_4$ nanocrystals.

1.11.2 Mn-Zn Ferrite Synthesis under Flow-Rate-Controlled Conditions

1.11.2.1 XRD Measurements

In these experiments, the Mn+Zn ionic solution was added to the NaOH one at fixed flow-rate controlled by a micro-peristaltic pump. Figure 33 shows the XRD patterns for $\text{Mn}_{0.8}\text{Zn}_{0.2}\text{Fe}_2\text{O}_4$ ferrites powders produced after 1 hour of reaction. The flow-rate of the addition of reactants varied between 1mL/min and 20 mL/min. For comparison purposes, the pattern for the solid produced with no control on flow-rate (‘0’ mL/min) is also presented.

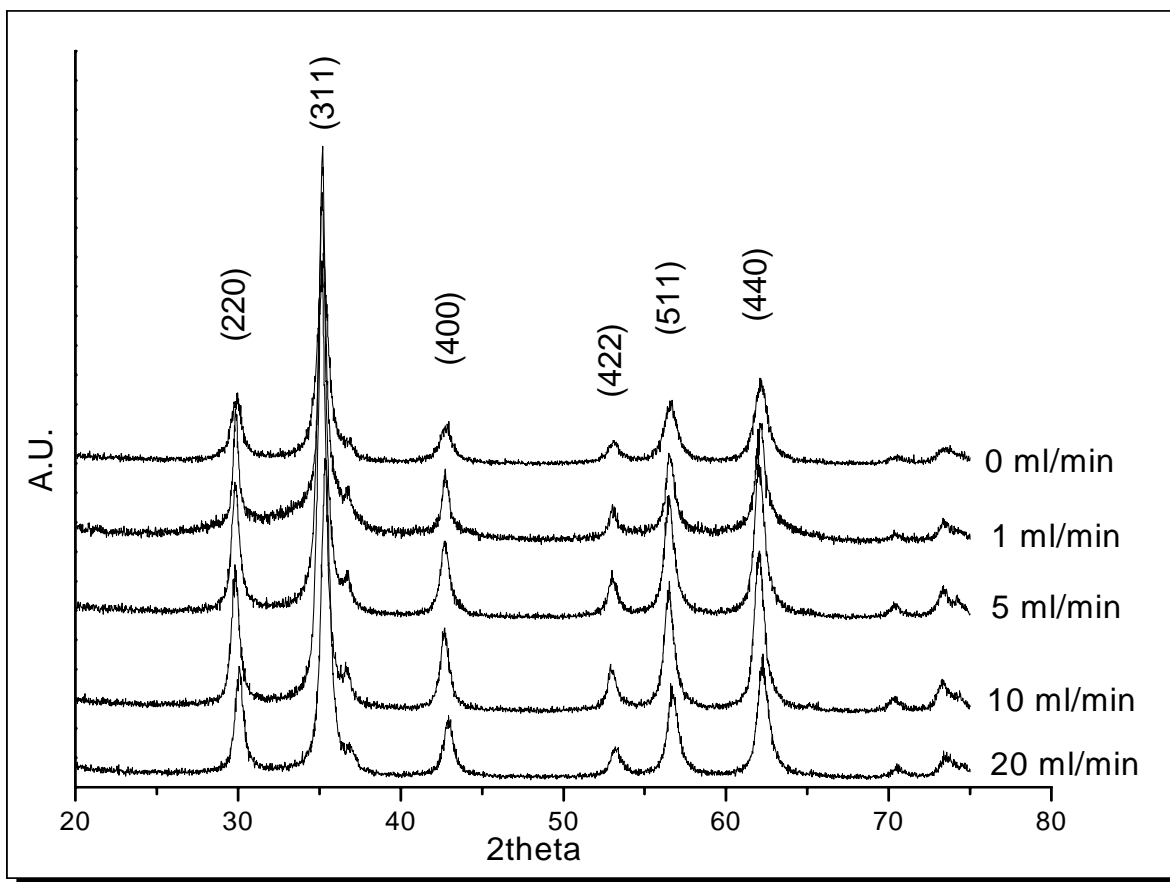


Figure 33. XRD patterns for Mn-Zn ferrites, $x=0.8$ for Mn, synthesized under intensive heating and different flow-rate of the addition of the reactants. For comparison purposes, the pattern for the solid produced with no control on flow-rate ('0' mL/min) is also presented.

All XRD peaks correspond to the ferrite structure, evidencing the formation of this material irrespective the way how the Mn-Zn solution is contacted with boiling NaOH. The average crystallite size varied from 15nm to 20nm when the flow-rate was increased from 1mL/min to 20mL/min, respectively. These values were larger than those determined for the ferrite synthesized with no control on the flow rate. The difference came because with the flow-rate controlled conditions,

we tried to promote the growth of the particle. Ferrite nuclei, quickly formed at the earlier stages of the reaction, would have acted as seeds that promoted the heterogeneous nucleation by incorporating of additional Mn, Zn and Fe species. The corresponding lattice parameter, 'a', did not exhibited a noticeable variation (0.831nm - 0.832nm) for the evaluated flow-rates.

Flow Rate (ml/min)	Average Crystallite size(nm) +/- 0.1	a (nm) +/- 0.002
0	10.6	0.830
1	19.8	0.831
5	14.9	0.832
10	14.9	0.832
20	13.2	0.827

Tabla 7. Average Crystallite size and lattice parameter as a function of the differents value of the flow rate.

1.11.2.2 Magnetic Characterization

Our previous work on the synthesis of Mn-Zn ferrite nanocrystals under flow-rate controlled conditions verified the viability in enhancing the average crystal size, which should be conducive to a rise in the magnetization of the samples. Accordingly, the M-H measurements were conducted on those nanocrystals produced at different flow-rates in the 1mL/min-20mL/min range. The corresponding results are shown in

figure 34. The Mn atomic fraction, 'x', was 0.8 and the reaction time 1 hour. As table 8 shows the magnetization values exhibited a rising trend when the flow-rate was increased in the selected interval. The magnetization was increased from 49 emu/g up to 59 emu/g. Evidently, the rise in magnetization can be attributed to the small, but noticeable crystal growth in which single domain crystals are formed under flow-rate controlled synthesis conditions. In the plot, '0 mL/min' means the magnetization data for the solid produced without control of the flow-rate of reactants addition.

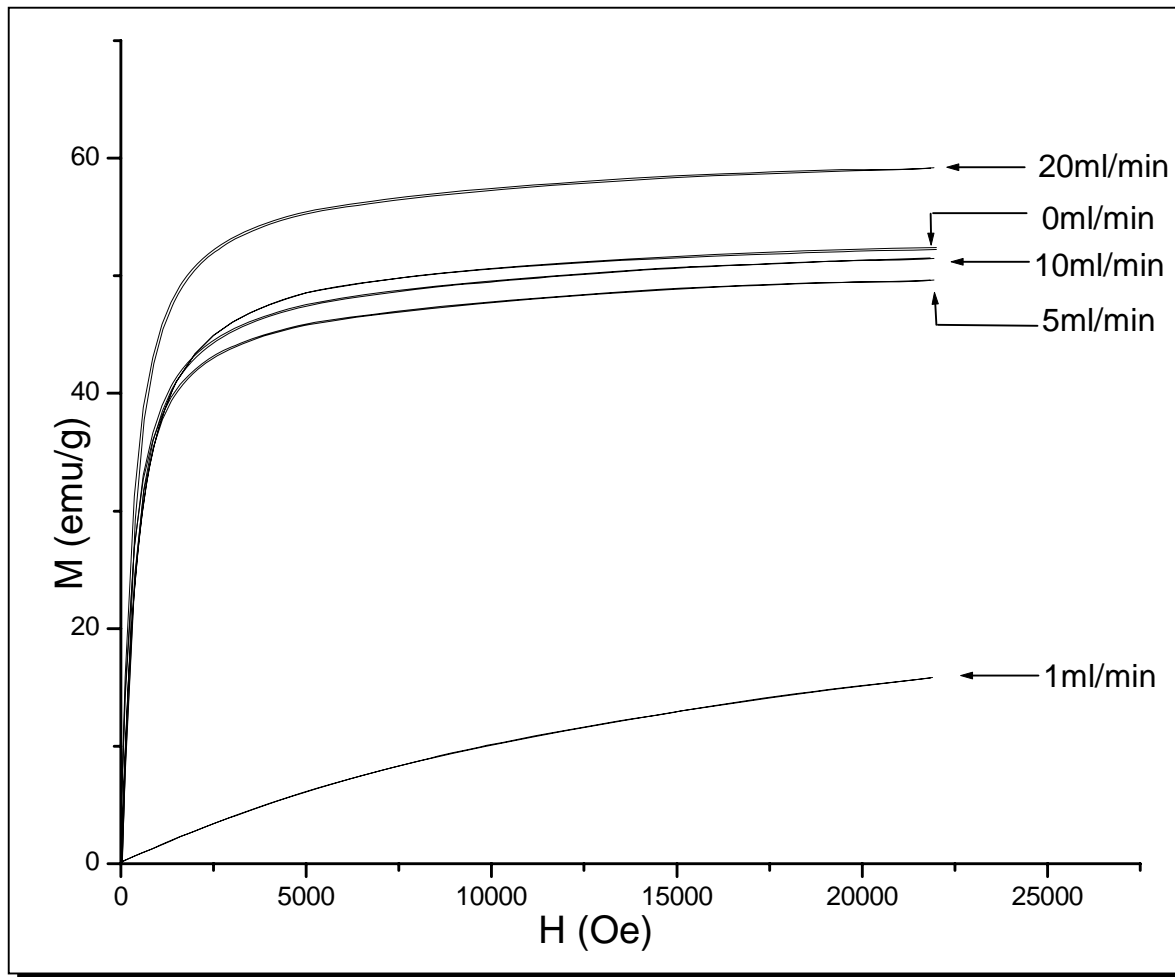


Figure 34. Room temperature M-H Curves for Mn-Zn ferrites ($x=0.8$) synthesized under flow-rate controlled conditions. '0' mL/min corresponds to the solid produced with no control of the flow rate of reactant addition.

Flow Rate (ml/min)	Average Crystallite size (nm) +/- 0.1	M _{Max} (emu/g) +/- 1
0	10.6	52
1	19.8	15
5	14.9	49
10	14.9	51
20	13.2	59

Tabla 8. Average crystallite size and maximum magnetization as a function of the flow rate of reactants additions.

On a general basis, the control on flow-rate of the reactants additions allowed a rise in the average crystallite size up to 20nm (1mL/min). However, the magnetization observed at this particular flow-rate (15 emu/g) was too low. It can be explained by the incomplete conversion of the paramagnetic intermediate (a combined hydroxide of Fe, Mn and Zn) into the anhydrous ferrite. This poorly crystalline intermediate could not be identified by XRD measurements. The maximum magnetization of 59 emu/g was attained for 20mL/min of flow-rate. In this case, the heterogeneous nucleation (i.e, crystal growth, as suggested by XRD measurements) promoted by the control in the oversaturation conditions during the ferrite formation, could explain this rise in magnetization. This magnetization was higher than others reported in the literature [7].

M-T measurements

Figure 35 shows the variation of magnetization with temperature for the Mn-Zn ferrite nanocrystals ($x=0.8$) synthesized at a flow-rate of reactants addition of 20mL/min. We selected this flow-rate because it provided the highest magnetization. The M-T data was collected under an external magnetic field of 2.2 T using VSM. The T_C value decreased from 675K (no control on flow-rate) down to 591K (20 mL/min). Although it is expected a rise in the magnetization (as verified in the M-H measurements) the drop in T_C was not expected on the consideration that a constant chemical composition should have been maintained by the ferrite. Furthermore, the pyromagnetic coefficient was also increased from 0.16emu/g-K up to 0.34emu/g-K under flow-rate controlled synthesis conditions.

Although still unclear, the drastic drop in T_C could be attributed to the change in the chemical composition of the ferrite induced by the flow-rate controlled synthesis conditions or to the rearrangement of Mn and Fe atoms in the ferrite sites. In previous work the flow rate process do not affect the T_C values around 585K [7]. In our research we decrease the T_C values from 675K to 591K. Further research using Mossbauer spectroscopy could provide additional insights on the actual reasons behind this behavior.

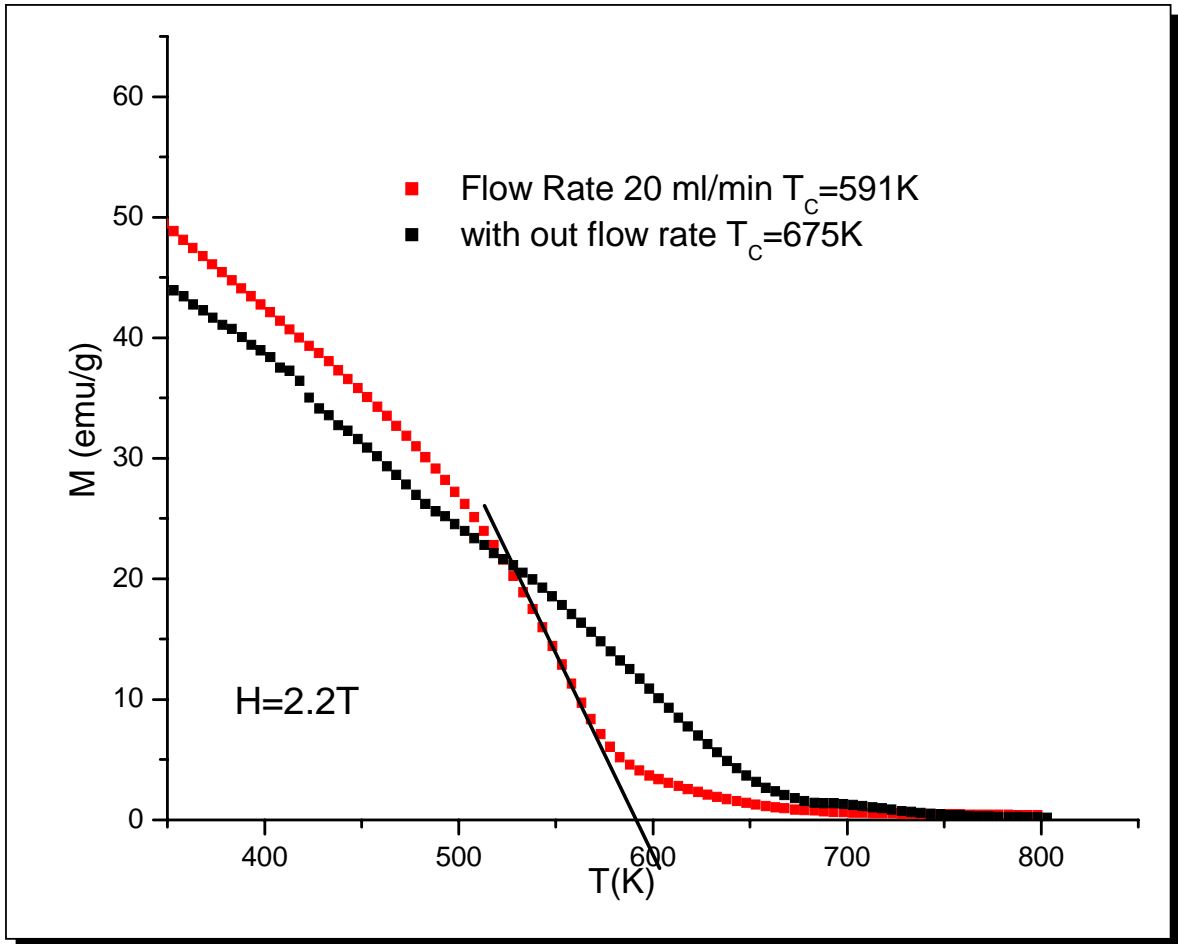


Figure 35. M-T Curves for Mn-Zn ferrites for different rate addition of ionic solutions "flow rate control". The external magnetic field was 2.2T.

1.12 GADOLINIUM -DOPED M_N - Z_N FERRITE NANOCRYSTALS

1.12.1 Conventional co-precipitation synthesis of $Mn_xZn_{1-x}Fe_{2-y}Gd_yO_4$ nanocrystals

1.12.1.1 XRD Measurements

Figure 36 shows the XRD patterns for Gd-doped $Mn_{0.8}Zn_{0.2}Gd_yFe_{2-y}O_4$ ferrites for a dopant atomic fraction of Gd, 'y' between 0.01 and 0.1. The reaction time was 4 hours. The excellent matching between the angular positions of the diffraction peaks of doped-ferrites with those corresponding to the undoped one, suggested that Gd^{3+} (ionic radii 0.97 Å) would have substituted Fe^{3+} ions (0.64 Å) in the host structure, at least for the evaluated range of rare-earth ion concentration.

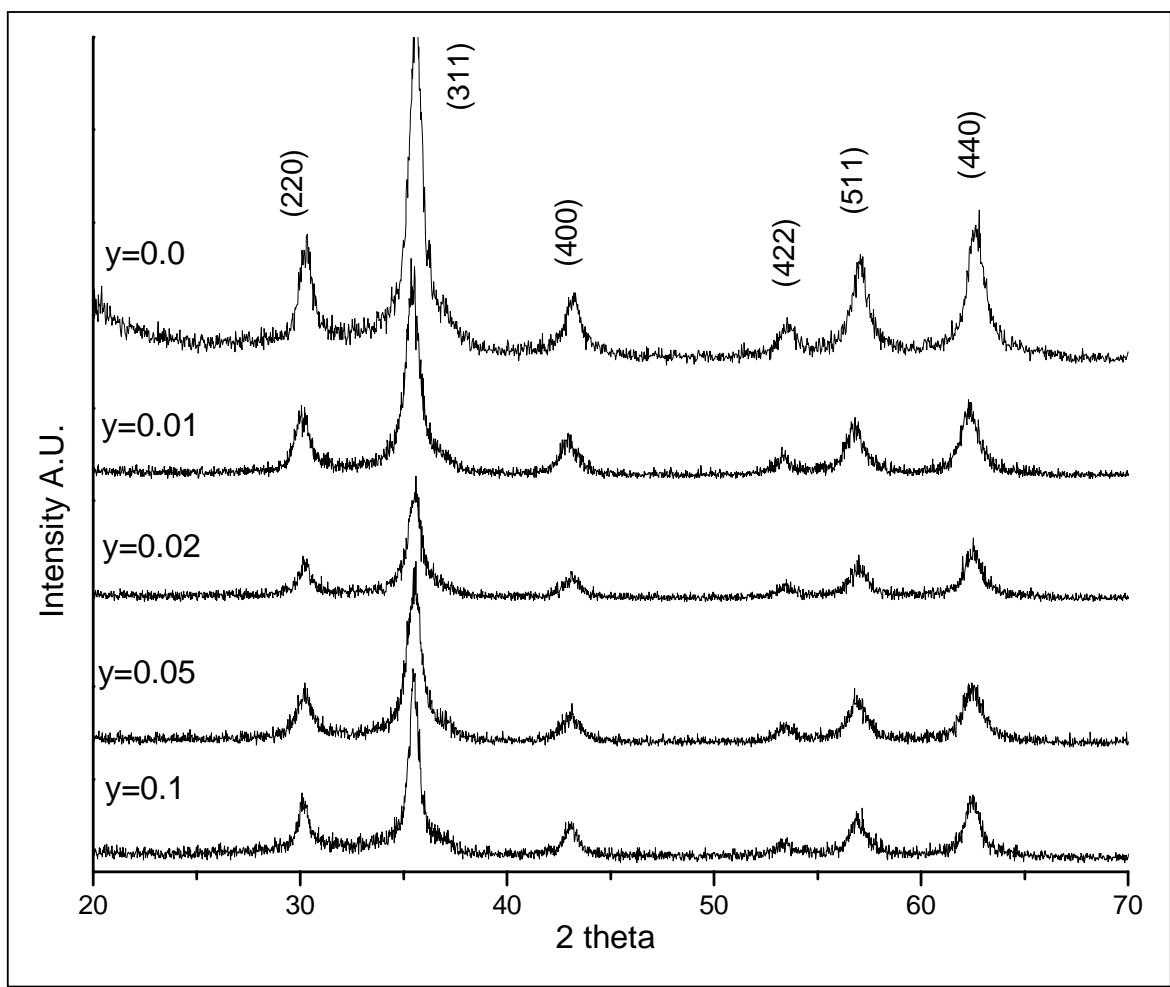


Figure 36. XRD patterns for Gd-doped $\text{Mn}_{0.8}\text{Zn}_{0.2}\text{Gd}_y\text{Fe}_{2-y}\text{O}_4$ synthesized on a hot plate and at different Gd atomic fractions, 'y'.

The average crystallite size, estimated by applying the Debye-Scherrer's equation for the (311) peak, varied between 13 and 20nm, when the fraction of Gd ions, 'y', was increased from 0.01 to 0.1. If we compare the average crystallite sizes of the one un-doped (11nm) with the doped one a small increase in these parameters it is evident. We can attribute these characteristic to the presence of small amount of dopant species, which may have changed the stability conditions of the intermediate

(mixed hydroxide) compound. The corresponding lattice parameter, 'a', was slightly increased from 0.836nm +/-0.002nm to 0.838nm +/-0.002nm for 'y' 0.01 and 0.1, respectively. These Values are slightly larger than the 'a' parameter for the un-doped (y=0) ferrite (0.830nm +/-0.002nm). This slight distortion in the unit cell could be due to substitution of Fe³⁺ ions (0.64 Å) by Gd³⁺ (ionic radii 0.97 Å) and Eu³⁺ (0.98 Å) species in the host ferrite structure. Table 9 presents the average crystallite size and lattice parameter as function of the atomic fraction of Gd dopant, 'y'.

Gd atomic fraction, 'y'	Average crystallite size +/- 0.1nm	'a' +/- 0.002nm
0	10.9	0.830
0.01	10.4	0.824
0.02	12.7	0.822
0.05	11.8	0.825
0.1	16.3	0.824

Tabla 9. Average crystallite size and lattice parameter, 'a', variation as a function of the Gd atomic fraction, 'y' in Mn_{0.8}Zn_{0.2}Gd_yFe_{2-y}O₄ nanocrystals.

1.12.1.2 Magnetic Characterization

i. M-H measurements

A Mn atomic fraction 'x' of 0.8 was selected based on the previous results about the effect of atomic fraction on Mn ions on the magnetic properties of the ferrite. Figure 37 shows the M-H curves for Gd-doped

Mn-Zn ferrites. The curve for the ferrite without Gd, i.e., 'y' = 0, is also included for comparison purposes, only.

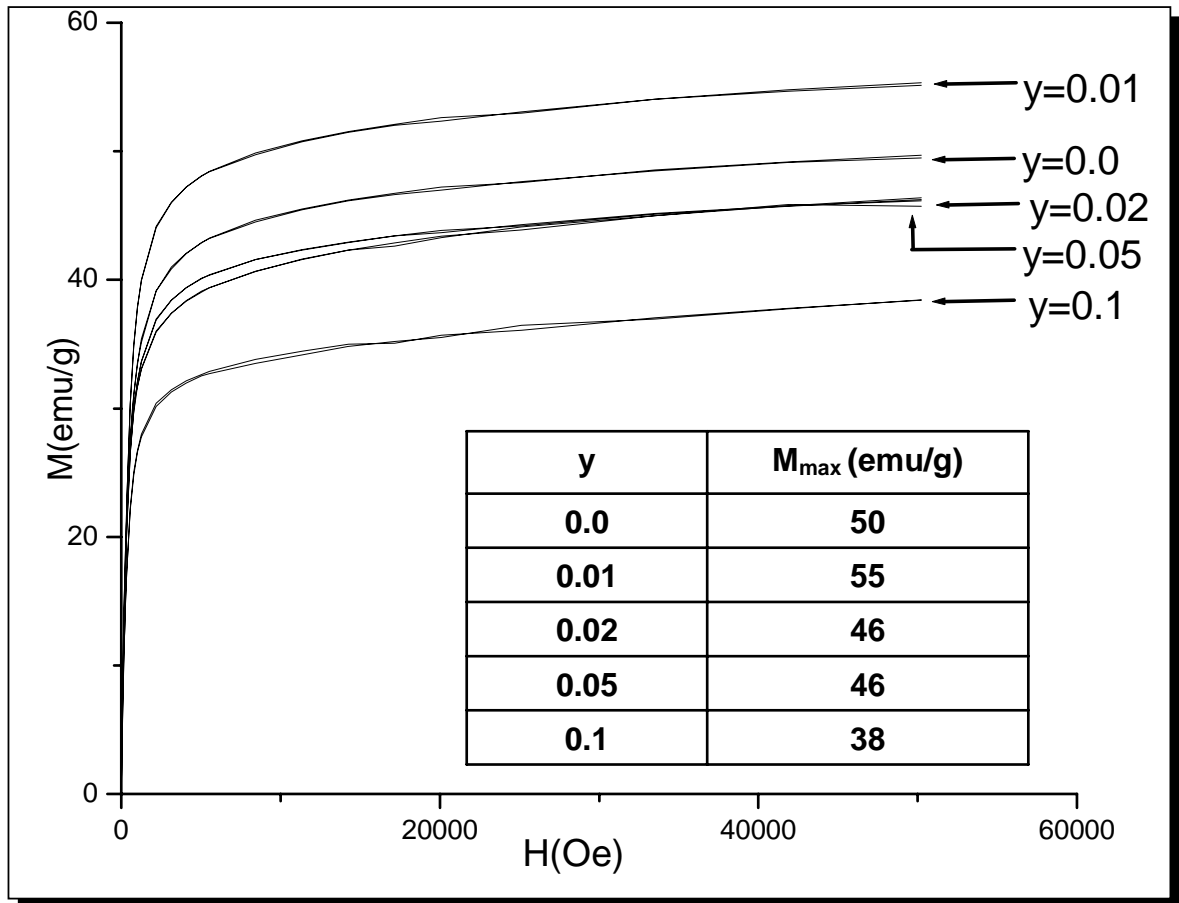


Figure 37. Room temperature M-H curve for Gd-doped $Mn_{0.8}Zn_{0.2}Fe_{2-y}Gd_yO_4$ at different Gd atomic fraction, 'y'. The inset shows the Maximum Magnetization values for different the atomic fractions of Gd, 'y'.

As a general trend it was observed that the higher the Gd fraction in the Mn-Zn ferrite the lower the maximum magnetization of the solids. Moreover, the M-H profiles do not look saturated, which could be due to the presence of an important fraction of superparamagnetic particles. An exception to the mentioned trend in the magnetization was observed for

'y'= 0.01; the magnetization was 55 emu/g in contrasts with the 50 emu/g observed for the undoped ferrite. This rise in magnetization can be explained by substitution of Fe^{3+} by Gd^{3+} ions, having a higher magnetic moment, in B-sites. Upadhyay et al. [2] has attributed this variation in magnetization to the enhancing effect on the inter-sublattice exchange energy between Mn-O-Gd and Mn-O-Fe, with respect to the Fe-O-Fe interaction in the ferrite lattice. Our results are different to what has been suggested for bulk ferrites. In our case, the presence of minor amounts of Gd ($y=0.01$) caused a rise in the maximum magnetization at 5T. This increase on magnetization could be due to the atomic rearrangement of Fe and Gd ions between the A and B sites in the ferrite. Moreover, the enlargement on crystallite size as observed in the Gd (0.01)-doped Mn-Zn ferrite powders, as suggested by XRD measurements, can also be involved with this change in magnetization. The magnetization of the ferrites went down when a larger fraction of Gd species were used. The reasons behind this variation in magnetization, besides the probable crystal size effect, are still unclear and further research must be done to clarify this point.

Distortion of the ferrite structure by the incorporation of dopants with ionic radii larger than host iron ions could also be related with the observed drop in magnetization. Mossbauer spectroscopy measurements

should be considered to get additional information on how the magnetic environment of Fe ions changes with the incorporation of the dopant species.

ii. Magnetization-Temperature measurements for doped $\text{Mn}_{0.8}\text{Zn}_{0.2}\text{Fe}_2\text{O}_4$ ferrite nanocrystals

The linear part of the variation in magnetization with temperature plots, measured by SQUID at 7 Tesla, for Gd-doped $\text{Mn}_{0.8}\text{Zn}_{0.2}\text{Fe}_2\text{O}_4$ ferrite nanocrystals are shown in Figures 38. The pyromagnetic coefficient, estimated from the slope of the M-T data for the Gd atomic fraction of 0.02, was 0.16emu/g-K, which was slightly above the value for the other compositions (0.14emu/g-K). For the ferrite with out Gd the pyromagnetic coefficient was 0.09emu/g-K, then, the incorporation of the rare-earth dopant increase the pyromagnetic coefficient, in the evaluated temperature range, although with a drop in magnetization. Table 10 present the pyromagnetic coefficient values for the Gd-doped Mn-Zn ferrites, calculate by M-T corresponding curves.

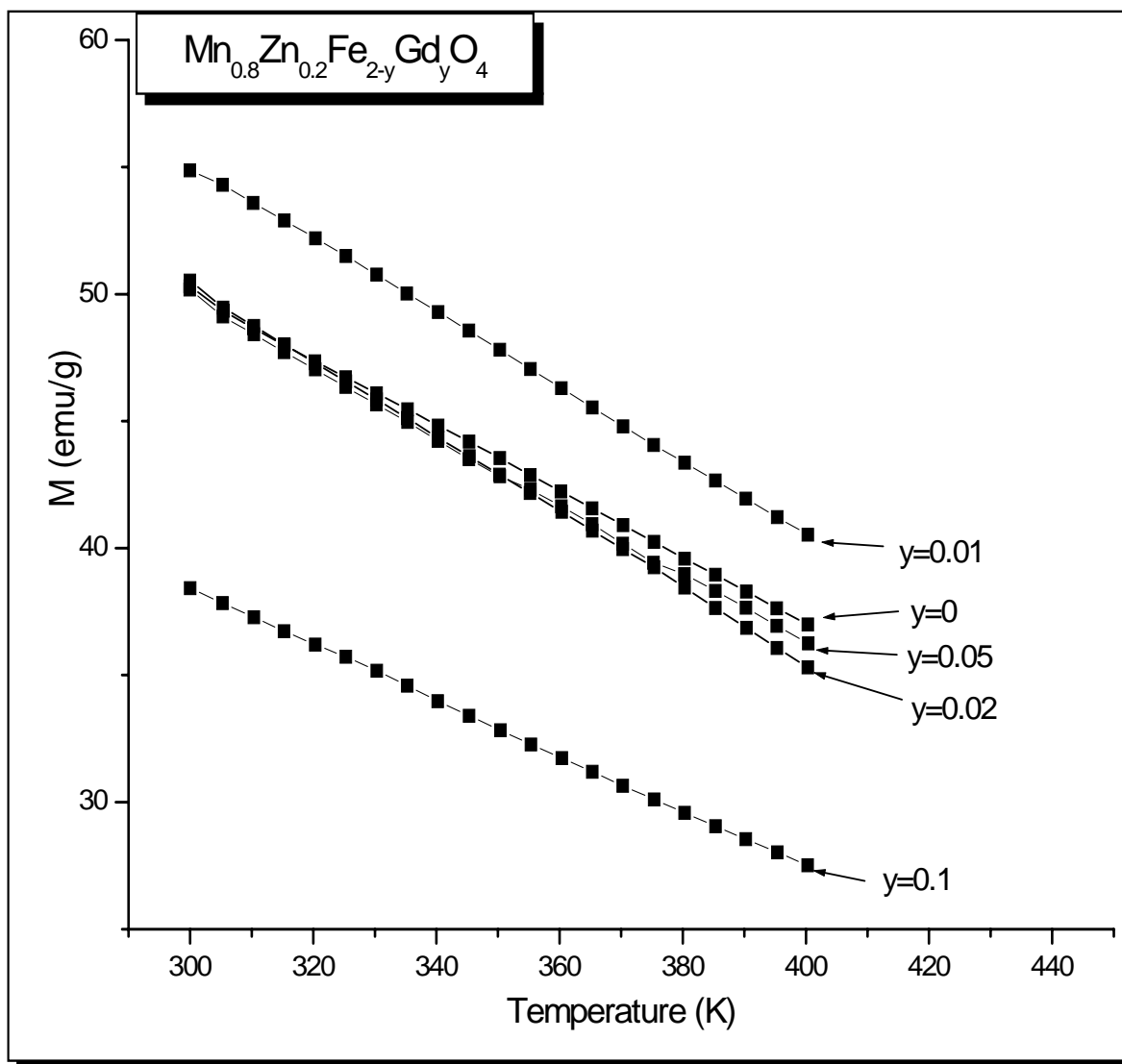


Figure 38. M-T plots for $Mn_{0.8}Zn_{0.2}Fe_{2-y}Gd_yO_4$ ferrites at different Gd atomic fractions, 'y'. The external magnetic field was 7 T.

Gd 'y'	Pyromagnetic coefficient (emu/g-K) +/- 0.01
0.0	0.09
0.01	0.14
0.02	0.16
0.05	0.14
0.1	0.11

Tabla 10. Technical Curie temperature as a function of the atomic fraction of Gd ions, 'y'.

A Gd atomic fraction was selected, 'y', of 0.01 to investigate the variation of magnetization with temperature for the whole range of temperatures. For this purpose, a VSM unit was used instead of SQUID. The external magnetic field was 2.2 T. The M-T plots of figure 39 correspond to the Mn-Zn ferrite nanocrystals with $x=0.8$, with and without Gd dopants ($y=0.01$). The most important results were the rise in the pyromagnetic coefficient and the drop in the T_C for the doped Gd-doped ferrite. The T_C went down from 675K (without Gd-doping) to 600K (with 0.01 Gd). The corresponding pyromagnetic coefficients were 0.15 emu/g-K and 0.27 emu/g-K, respectively. This variation in the T_C values was also observed in ceramic ferrites doped with rare earth ions [38]. In our case, the variation in T_C and the pyromagnetic coefficient with doping of Mn-Zn ferrite nanocrystals by Gd species is presented

here for the first time. The combination of decrease in T_C , rise of the pyromagnetic coefficient without affecting the magnetization will be very important to optimize the efficiency of the magnetocaloric pumping system that will use our materials.

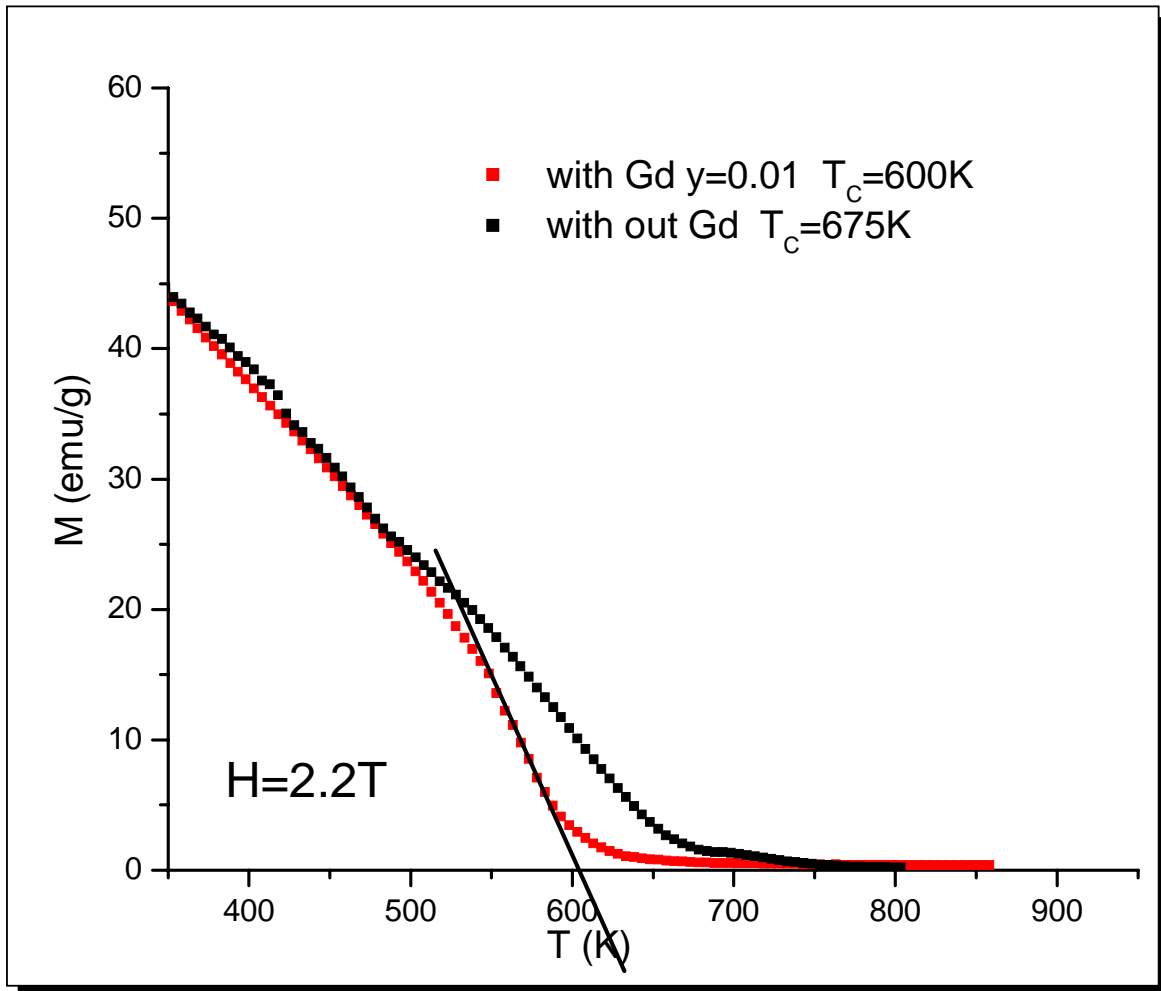


Figure 39. M-T plots for Mn(0.08)-Zn ferrites with and without Gd ions ($y=0.01$). The external magnetic field was 2.2 T.

1.12.2 Flow-rate Controlled Synthesis of $\text{Mn}_{0.8}\text{Zn}_{0.2}\text{Fe}_{1.99}\text{Gd}_{0.01}\text{O}_4$ ferrite nanocrystals

1.12.2.1 XRD Measurements

Additional synthesis were carried out in presence of Gd (III) in starting reacting solutions to take advantage of the control of flow rate on the enhancement on crystal size. Figure 40 shows the XRD patterns for $\text{Mn}_{0.8}\text{Zn}_{0.2}\text{Fe}_{1.99}\text{Gd}_{0.01}\text{O}_4$ ferrites powders produced after 1 hour of reaction time and different flow-rates of reactants addition (1ml/min-20ml/min). Also in this case, all reflections correspond to the ferrite structure. The average crystallite size varied from 12nm up to 18nm by increasing the flow-rate from 1mL/min to 20ml/min. As in the case of the Mn-Zn ferrite nanocrystals, the promoting effect of the control of flow-rate on the average crystallite size was evidenced. The solid produced at 20ml/min exhibited an average crystallite size (18nm) larger than the one corresponding to the solid produced with no control of flow-rate (11nm).

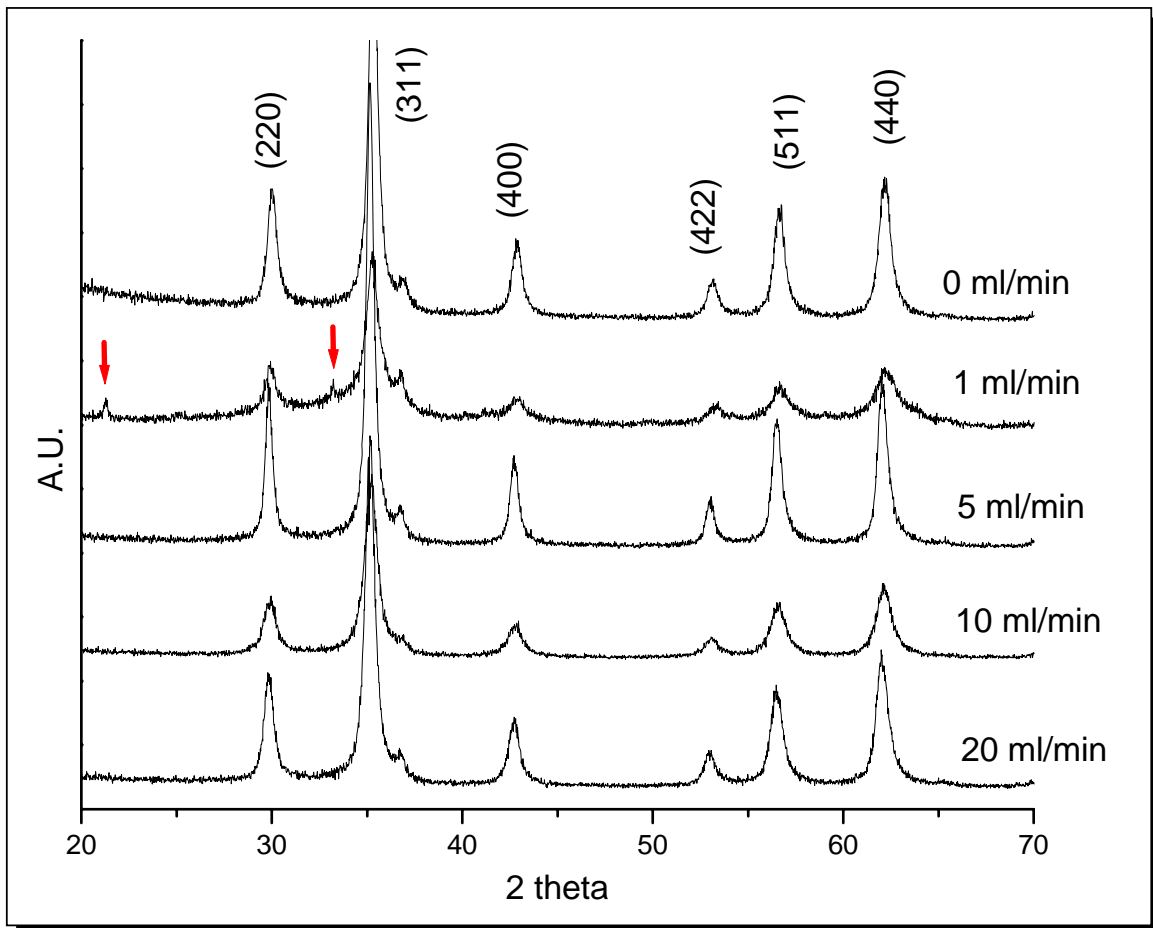


Figure 40. XRD patterns for $Mn_{0.8}Zn_{0.2}Gd_yFe_{2-y}O_4$ doped with Gd $y=0.01$, synthesized at different flow rate of the reactants addition.

The control of over saturation conditions of the solution, achieved by controlling the flow-rate of reactant addition, should have favored crystal growth; initially formed nuclei could have acted as pre-existent seeds that promoted heterogeneous nucleation. For a flow rate of 1ml/min XRD patterns were observed that did not correspond to the peaks of the spinel structure of the ferrite. The peak's widths suggest poor crystalline ferrite and also very small particles. The reduced

saturation condition caused by the low flow rate values (1ml/min) probably affects the stability of the ferrite producing other contained structure.

Flow Rate (ml/min)	Average Crystallite size(nm) +/- 0.1	a (nm) +/- 0.002
0	10.6	0.830
1	11.5	0.829
5	17.7	0.832
10	15.1	0.828
20	14.1	0.832

Tabla 11. Average crystallite size and lattice parameter as a function of the flow rate for Gd-dope ($y=0.01$) ferrite.

Table 11 presents a summary of the variation in average crystallite size and the lattice parameter, 'a', in $Mn_{0.8}Zn_{0.2}Fe_{1.99}Gd_{0.01}O_4$ with the flow-rate of reactants addition. For comparison purposes, the sample produced without control of flow-rate, '0' ml/min, is also included. The corresponding lattice parameter, 'a', was slightly increased from 0.829nm to 0.832nm when the flow rate varied between 1ml/min and 20ml/min. The lattice parameter is around 0.830nm that is smaller than the obtained 0.836nm for the Gd-doped ferrite with flow rate.

1.12.2 Magnetic Characterization of $\text{Mn}_{0.8}\text{Zn}_{0.2}\text{Fe}_{1.99}\text{Gd}_{0.01}\text{O}_4$ ferrite nanocrystals

i. M-H measurements

Previous data suggested that both the increase in magnetization and the decrease in T_C could be achieved not only by suitable selection of the Mn-Zn ferrite composition but also by a suitable control of the flow-rate of reactants addition to the boiling NaOH solution. Gd-doped Mn-Zn ferrite nanocrystals ($x=0.8$, $y=0.01$) synthesized at flow-rates between (1mL/min-20 mL/min) were characterized by VSM. Figure 41 shows the M-H profiles at room temperature of the mentioned Gd-doped Mn-Zn ferrite nanocrystals. The profiles were more saturated than those obtained in undoped Mn-Zn ferrites; it may suggest a reduced amount of superparamagnetic particles. This fact was supported by the increase in the average crystallite size of the powders produced under flow-rate controlled synthesis conditions. The saturation magnetization values exhibited a systematic rising trend (from 20 emu/g up to 60 emu/g) when the flow-rate of reactants additions was increased from 1mL/min to 20 mL/min. The 'zero mL/min' condition represents the M-H data for the ferrite synthesized with no control of the flow-rate. The Gd-doped Mn-Zn ferrite nanocrystals ($x=0.8$, $y=0.01$) synthesized with no control on flow-rate reported a saturation magnetization of 52 emu/g for an

average crystallite size of 11nm. This size was increased up to 14nm when 20ml/min was used instead; the corresponding saturation magnetization was increased up to 60 emu/g. This variation in magnetization is attributed to the enhancement on crystal growth by higher flow-rates of reactants addition, as suggested by XRD analyses.

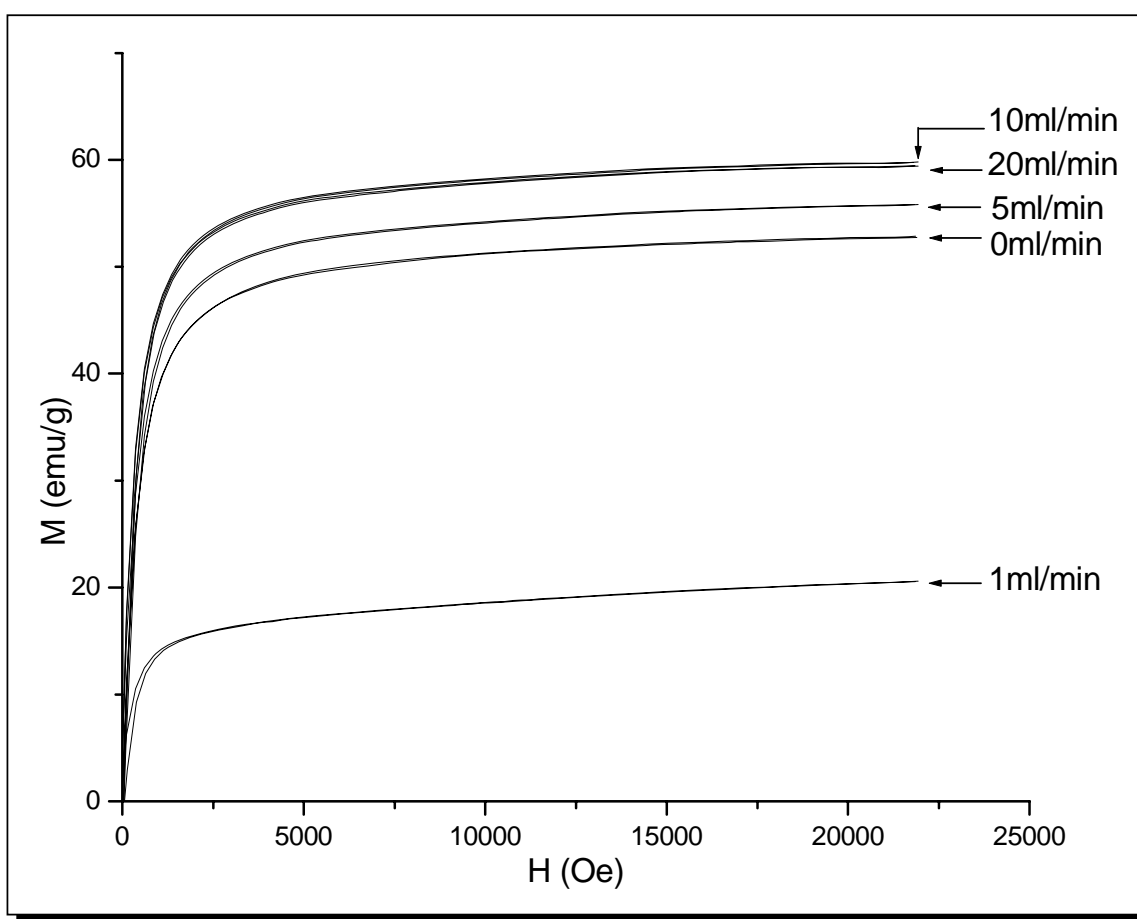


Figure 41. Room temperature M-H Curves for Mn(0.08)-Zn ferrites doped with Gd and synthesized at different flow-rates

ii. M-T measurements

Figure 42 compares the M-T profiles for Gd-doped Mn-Zn ferrite ($x=0.8$, $y=0.01$) synthesized at a flow rate of 10ml/min, with the same ferrite and the Mn-Zn ferrite without Gd, synthesized without any control on the flow-rate. The flow-rate of the reactants additions did not affect the T_C of the Gd-doped ferrites so drastically (it varied from 604K, no flow-rate, to 617K at 10ml/min T_C for the MN-ferrite without Gd dopants was 675K) and also do not the pyromagnetic coefficient (0.27 emu/g-K and 0.24 emu/g-K, respectively). The most remarkable effect of the flow-rate on the magnetic properties of the Gd-doped ferrite was that the particles exhibited a rise in magnetization when compared with the powders synthesized without flow-rate control. Therefore, the drop in T_C and the rise in magnetization, two of our main goals within this research, can be achieved by suitable control of the ferrite composition ($x=0.8$, $y=0.01$) and careful control of the oversaturation conditions during the ferrite formation in aqueous phase; the later, provided by the control on the flow-rate of reactants additions. These two conditions, high magnetization and low T_C , are crucial for the envisioned application of the ferrite nanocrystals fundamental in the magnetocaloric pumping systems, as discussed in section 2.1.3.

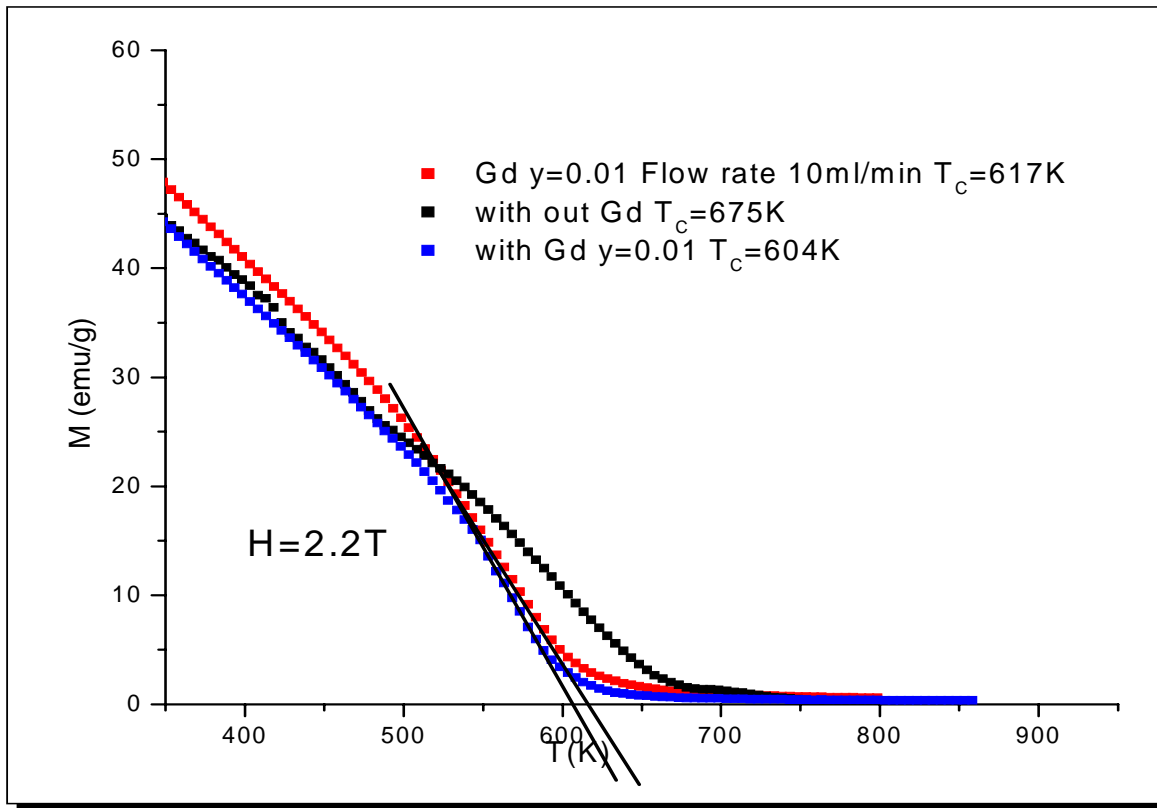


Figure 42. M-T Curves for Mn-Zn ($x=0.8$, $y=0$) ferrite nanocrystals and Gd-doped Mn-Zn ferrite nanocrystals ($x=0.8$, $y=0.01$) synthesized with and without control on flow-rate (10mL/min). The external magnetic field was 2.2 T.

CONCLUDING REMARKS

We have verified the tuning on the magnetic properties of the Mn-Zn ferrite nanocrystals by a suitable control of both, composition and crystal size at the nanoscale. Mn-Zn ferrite nanoparticles with FCC structure have been synthesized by conventional co-precipitation method. With this method it was obtained nanoparticles with approximately 9 nm to 16nm diameter and poly-disperse distribution. The maximum magnetization of Mn-Zn ferrite nanocrystals was strongly dependent on the 'x' value and varied from 13 emu/g to 59 emu/g when 'x' was increased from 0.0 to 1.0, respectively. The T_c values were also dependent on the composition of the Mn-Zn ferrite. This value varied between 559K and 695K when 'x' varied from 0.5 to 1.0, respectively. The applied magnetic field was 2.2T.

The presence of rare earth (RE) dopant like Gd affect the structure and the magnetic properties like M_s , T_c and the pyromagnetic coefficient of the particles. Depending of the atomic fraction of the Gd species, the maximum magnetization of the doped ferrite was as high as 55 emu/g for a Mn (0.08)-Zn ferrite.

The control of the flow-rate of reactants should have modified oversaturation conditions favoring the crystal growth. Under optimum

conditions the bare and the Gd-doped Mn-Zn ferrite nanocrystals were enlarged from 11nm up to 18nm. Furthermore, the variation in crystal size by controlling the flow-rate of reactants addition was also conducive to a variation in the corresponding T_c values.

It was observed a reduction in the T_c values when the syntheses were carried out under flow-rate controlled conditions. The technical T_c values went down from 675K (no-control on flow-rate) to 591K (20 ml/min) for Mn(0.08)-Zn ferrite. The corresponding pyromagnetic coefficient was also increased from 0.15 emu/g-K up to 0.27 emu/g-K. This is a very important aspect for the application of the produced ferrite nanocrystals in the magnetocaloric pumping system.

Additional work on the atomic distribution and magnetic structure of the Gd-doped Mn-Zn ferrites will be required to get a deeper understanding of the observed effects. Produced ferrites will be used to prepare magnetic fluids for the magnetocaloric pumping prototype.

APPENDIX A

Chemical composition by Inductively coupled plasma (ICP) analysis.

ICP Result

Ferrite atomic fraction of Mn $x=0.9$		
Metal	mg/kg	%RSD
Mn	1.44E+05	0.75
Fe	2.66E+05	0.76
Zn	1.60E+04	1.24
Ferrite atomic fraction of Mn $x=0.8$		
Metal	mg/kg	%RSD
Mn	1.54E+05	8.89
Fe	3.31E+05	9.31
Zn	4.48E+04	9.12
Ferrite atomic fraction of Mn $x=0.8$ Flow Rate 20ml/min		
Metal	mg/kg	%RSD
Mn	1.38E+05	3.80E-01
Fe	2.94E+05	2.80E-01
Zn	4.10E+04	4.30E-01

Tabla 12. ICP general data fr MN-Zn ferrite nanocrystals.

ICP analysis $\text{Mn}_{0.9}\text{Zn}_{0.1}\text{Fe}_2\text{O}_4$

Theoretical Molar Ratio

$$\frac{\text{Mn}}{\text{Zn}} = \frac{0.9}{0.1} = 9$$

Experimental Molar Ratio

$$\frac{\text{Mn}}{\text{Zn}} = \frac{\left[\frac{1.44 \times 10^5 \text{ mg / kg}}{54.94 \text{ mg / mmol}} \right]}{\left[\frac{1.60 \times 10^4 \text{ mg / kg}}{65.39 \text{ mg / mmol}} \right]} = 11$$

Theoretical Molar Ratio

$$\frac{\text{Fe}}{\text{Zn}} = \frac{2}{0.1} = 20$$

Experimental Molar Ratio

$$\frac{\text{Fe}}{\text{Zn}} = \frac{\left[\frac{2.66 \times 10^5 \text{ mg / kg}}{55.94 \text{ mg / mmol}} \right]}{\left[\frac{1.60 \times 10^4 \text{ mg / kg}}{65.39 \text{ mg / mmol}} \right]} = 19$$

Theoretical Molar Ratio

$$\frac{Fe}{Mn} = \frac{2}{0.9} = 2.2$$

Experimental Molar Ratio

$$\frac{Fe}{Mn} = \frac{\left[\frac{2.66 \times 10^5 \text{ mg / kg}}{55.94 \text{ mg / mmol}} \right]}{\left[\frac{1.44 \times 10^5 \text{ mg / kg}}{54.94 \text{ mg / mmol}} \right]} = 1.8$$

ICP analysis $Mn_{0.8}Zn_{0.2}Fe_2O_4$

Theoretical Molar Ratio

$$\frac{Mn}{Zn} = \frac{0.8}{0.2} = 4$$

Experimental Molar Ratio

$$\frac{Mn}{Zn} = \frac{\left[\frac{1.54 \times 10^5 \text{ mg / kg}}{54.94 \text{ mg / mmol}} \right]}{\left[\frac{4.48 \times 10^4 \text{ mg / kg}}{65.39 \text{ mg / mmol}} \right]} = 4$$

Theoretical Molar Ratio

$$\frac{Fe}{Zn} = \frac{2}{0.2} = 10$$

Experimental Molar Ratio

$$\frac{Fe}{Zn} = \frac{\left[\frac{3.31 \times 10^5 \text{ mg / kg}}{55.94 \text{ mg / mmol}} \right]}{\left[\frac{4.48 \times 10^4 \text{ mg / kg}}{65.39 \text{ mg / mmol}} \right]} = 9$$

Theoretical Molar Ratio

$$\frac{Fe}{Mn} = \frac{2}{0.8} = 2.5$$

Experimental Molar Ratio

$$\frac{Fe}{Mn} = \frac{\left[\frac{3.31 \times 10^5 \text{ mg / kg}}{55.94 \text{ mg / mmol}} \right]}{\left[\frac{1.54 \times 10^5 \text{ mg / kg}}{54.94 \text{ mg / mmol}} \right]} = 2.1$$

ICP analysis Flow rate 20ml/min $Mn_{0.8}Zn_{0.2}Fe_2O_4$

Theoretical Molar Ratio

$$\frac{Mn}{Zn} = \frac{0.8}{0.2} = 4$$

Experimental Molar Ratio

$$\frac{Mn}{Zn} = \frac{\left[\frac{1.38 \times 10^5 \text{ mg / kg}}{54.94 \text{ mg / mmol}} \right]}{\left[\frac{4.10 \times 10^4 \text{ mg / kg}}{65.39 \text{ mg / mmol}} \right]} = 4$$

Theoretical Molar Ratio

$$\frac{Fe}{Zn} = \frac{2}{0.2} = 10$$

Experimental Molar Ratio

$$\frac{Fe}{Zn} = \frac{\left[\frac{2.94 \times 10^5 \text{ mg / kg}}{55.94 \text{ mg / mmol}} \right]}{\left[\frac{4.10 \times 10^4 \text{ mg / kg}}{65.39 \text{ mg / mmol}} \right]} = 8$$

Theoretical Molar Ratio

$$\frac{Fe}{Mn} = \frac{2}{0.8} = 2.5$$

Experimental Molar Ratio

$$\frac{Fe}{Mn} = \frac{\left[\frac{2.94 \times 10^5 \text{ mg / kg}}{55.94 \text{ mg / mmol}} \right]}{\left[\frac{1.38 \times 10^5 \text{ mg / kg}}{54.94 \text{ mg / mmol}} \right]} = 2.1$$

REFERENCES

1. R. E. Rosensweig, "Regenerative thermomagnetic power", *Journal of Energy and Power*. pp.399-406, 1967.
2. R.V. Upadhyay, R.V. Mehta, Kinnari Parekh, D. Sriniva, R.P. Pant, "Gd-substituted ferrite ferrofluid: a possible candidate to enhance pyromagnetic coefficient"; *J. Magn. Magn. Mater.*, vol. 201, pp. 129-132, 1999.
3. L. J. Love, J. F. Jansen, T. E. Mcknight, and T. J Phelps, "A magnetocaloric pump for micro-fluidic applications", *IEEE Transactions on nano-bioscience*, vol 3, n 2, 2004.
4. C. N. Chinnasamy, M. Senoue, B. Jeyadevan, Oscar Perales-Perez, K. Shinoda, K. Tohji, "Synthesis of size-controlled cobalt ferrite particles with high coercivity and squareness ratio", *J. Colloid Interface Sci*, vol. 263, pp. 80-83, 2004.
5. William D. Callister, *The University of Utah; Materials Science and Engineering 6th ed.*, Wiley 2003; R.E. Rosensweig, *Ferrohydrodynamics*, Dover, New York. 1997; R.E. Rosensweig, *Regenerative thermomagnetic power*. *Journal of Energy and Power*. pp. 399-406, 1967.
6. Brau, Charles A. (2004). *Modern Problems in Classical Electrodynamics*. Oxford University Press
Griffiths, David J. (1999). *Introduction to Electrodynamics*, 3rd ed., Prentice Hall
7. B. Jeyadevan, C.N. Chinnasamy, K. Shinoda, K. Tohji, "Mn-Zn ferrite

with higher magnetization for temperature sensitive magnetic fluid”, J Appl. Phys., vol. 93, pp. 8450-8452, 2003.

8. Permanent Magnets and Magnetism, edited by D. Hadfield, Liffé Books, LTD, London, John Wiley and Sons, Inc., New York, 1961.

9. Permanent Magnets and Their Applications, by Rollin J. Parker and Robert J. Studders, John Wiley and Sons, Inc., New York, 1962.

10. Advances in Permanent Magnetism, by Rollin J. Parker, John Wiley and Sons, Inc., New York, 1990.

11. Permanent Magnets in Theory and Practice, by Malcolm McCaig, John Wiley & Sons, Inc., Toronto, 1977.

12. Magnetism: From Lodestone to Polar Wandering, by D.S. Parasnis, Harper & Brothers, New York, 1961.

13. Richard M. Bozorth, Ferromagnetism, first published 1951, reprinted 1993 by IEEE Press, New York.

14. Kip Thorne, Spacetime Warps and the Quantum: A Glimpse of the Future, ITP & CalTech, 1999.

15. Electronic Materials Dr. Helmut Föll University of Kiel; Faculty of Engineering.

16. Shriver, D. F.; Atkins, P. W.; Overton, T. L.; Rourke, J. P.; Weller, M. T.; Armstrong, F. A. “Inorganic Chemistry” W. H. Freeman, New York, pp. 168-190, 2006.

17. A. Goldman, Modern Ferrite Technology. New York: Van Nostrand

Reinhold, 1990; N. Spaldin, *Magnetic materials: Fundamentals and device applications* Cambridge: Cambridge University press, 2003.

18. *Amorphous Magnetic Cores For High Frequency Electronics*, Hill technical, 2006.

19. K. Parekh, R.V. Upadhyay, R.V. Mehta. Magnetocaloric effect in temperature-sensitive magnetic fluids, *Bull. Mater. Sci*, pp. 90-94. 2000.

20. R. Arulmurugan, G. Vaidyanathan, S. Sendhilnathan, B. Jeyadevan. Mn-Zn ferrite nanoparticles for ferrofluid preparation: Study on thermal-magnetic properties, *J. Magn. Magn. Mater.*, vol. 298, pp. 83-94, 2006.

21. R.V. Upadhyay, R.V. Mehta, K. Parekh, D. Srinivas, R.P. Pant. Gd-substituted ferrite ferrofluid: a possible candidate to enhance pyromagnetic coefficient, *J. Magn. Magn. Mater.*, vol. 201, pp. 120-132, 1999.

22. T.N. Brusentsova, N. A. Brusentsov, V.D. Kuznetsov, V.N. Nikiforov. Synthesis and investigation of magnetic properties of Gd-substituted Mn-Zn ferrite nanoparticles as potential low-TC agent for magnetic fluid hyperthermia, *J J. Magn. Magn. Mater.*, vol. 293, pp. 115-118, 2005.

23. R. Arulmurugan, G. Vaidyanathan, S. Sendhilnathan, B. Jeyadevan. Co-Zn ferrite nanoparticles for ferrofluid preparation: Study on magnetic properties, *Physica B*. Vol. 363, pp. 225-231, 2005.

24. R. Arulmurugan, G. Vaidyanathan, S. Sendhilnathan, B. Jeyadevan. Thermomagnetic properties of $\text{Co}_{1-x}\text{Zn}_x\text{Fe}_2\text{O}_4$ ($x=0.1-0.5$) nanoparticles, *J. Magn. Magn. Mater.*, vol. 303, pp.131-137, 2006.
25. R. Joseyphus, A. Narayanasamy, K. Shinoda, B. Jeyadevan, K. Tohji. Synthesis and magnetic properties of the sizes-controlled Mn-Zn ferrite nanoparticles by oxidation method, *J. Phys. Chem. Solids*, vol. 67, pp.1510-1517, 2006.
26. J. Wang, C. Zeng, Z. Peng, Q. Chen. Synthesis and magnetic properties of $\text{Zn}_{1-x}\text{Mn}_x\text{Fe}_2\text{O}_4$ nanoparticles, *Physica B*, vol. 349, pp.97-103, 2004.
27. B. Skolyszewska, W. Tokarz, K. Przybylski, Z. Kakol. Preparation and magnetic properties of MgZn and MnZn ferrite, *Physica C*, vol. 387, pp.290-294, 2003.
28. E. Ateia, M.A. Ahmed, A.K. El-Aziz. Effect of rare earth radius and concentration on the structural and transport properties of doped Mn-Zn ferrite, *J. Magn. Magn. Mater.*, vol. 311, pp.545-554, 2007.
29. Yimin Xuan, Qiang Li, Gang Yang. Synthesis and magnetic properties of Mn-Zn ferrite nanoparticles, *J. Magn. Magn. Mater.*, vol. 312, pp.464-469, 2007.
30. "El Instituto de Ciencia de Materiales de Madrid" (ICMM). <http://www.icmm.csic.es/index.html>
31. Renteria-Beleño, Boris. Master Degree Thesis. University of Puerto

Rico at Mayagüez. "Preparation and Characterization of Polyaniline-Based Magnetic Nanocomposites for EMI Shielding Applications", 2007

32. C. R. Brundle, C. A. Evans Jr, S. Wilson. Encyclopedia of materials characterization, surfaces, interfaces, thin films, Butterworth-Heinemann a division of Reed Publishing CUSA Inc, pp. 198 - 201, 1992.

33. D. Jiles. Introduction to magnetism and magnetic materials. Chapman and Hall, 1st ed. pp.47 - 52, 1991.

34. D. Jiles, "Introduction to magnetism and magnetic materials", Chapman&Hall, Chapter 6, pp. 135-156, 1998.

35. N. Rezlescu, E. Cuciureanu, "Cation distribution and Curie temperature in some ferrites containing copper and manganese. Research Centre of Physics", Phys. Status Solidi A, vol. 3, Issue 4, pp. 873 - 878, 2006.

36. A.T. Rahavender, D. Pajic and K. Zadro. Synthesis and magnetic properties of $\text{NiFe}_{2-x}\text{Al}_x\text{O}_4$ nanoparticles, Department of Physics, Maratwada University, Maharashtra India. Unpublished.

37. Z.X.Tang, C.M.Sorensen, K.J.Klabunde, "Size-dependent Curie temperature in nano-scale MnFe_2O_4 particles", Phys. Rev. Lett. Vol.67 1991.

38. "Ceramicos magneticos" "Laboratorio de Fisicoquímica de Materiales Cerámicos Electrónicos" (LAFMACEL) in the Buenos Aires University

39. James F. Shackelford, University of California, Davis; Introduction to

Materials Science for Engineers, 4th ed., Prentice Hall, 1992.

40. Institute for Rock Magnetism University of Minnesota.

41. Soft and Hard Magnetic Materials Applied Alloy Chemistry Group, University of Birmingham.

42. L. J. Love, J. F. Jansen, T. E. Mcknight, Y. Roh, and T. J. Phelps, "A magnetocaloric pump for microfluidic applications", IEEE transactions on nanobioscience, vol 3, n 2, 2004.

43. M.S. Tomar, S.P. Singh, O. Perales, R.P. Guzman, E. Calderón, C. Rinaldi, "Synthesis and magnetic behavior of nanostructured ferrites for spintronics", Journal of Microelectronics , vol. 36, pp. 475-479, 2005.

44. B. Parvatheeswara Rao, O. Caltun, W.S. Choc, Chong-Oh Kim, CheolGi Kim "Synthesis and characterization of mixed ferrite nanoparticles", J. Magn. Magn. Mater., vol. 310, pp.812-814, 2007.

45. N. Chinnasamy, M. Senoue, B. Jeyadevan, Oscar Perales-Perez, K. Shinoda and K. Tohji "Synthesis of size-controlled cobalt ferrite particles with high coercivity and squareness ratio", J. Colloid Interface Sci., vol. 263, pp. 80-83, 2003.

46. Oscar Perales Perez, Yoshiaki Umetsu and Hiroshi Sasaki, "Precipitation and densification of magnetic iron compounds from aqueous solutions at room temperature", Hydrometallurgy, vol. 50, pp. 223-242, 1998.

47. R. Arulmurugan, B. Jeyadevan, G. Vaidyanathan and S.

Sendhilnathan. "Effect of zinc substitution on Co-Zn and Mn-Zn ferrite nanoparticles prepared by co-precipitation", J. Magn. Magn. Mater., vol. 288, pp. 470-477, 2005.